NEUROSCIENCE

Reticular thalamic hyperexcitability drives autism spectrum disorder behaviors in the Cntnap2 model of autism

Sung-Soo Jang, Fuga Takahashi, John R. Huguenard*

Copyright © 2025 The Authors, some rights reserved; exclusive licensee American Association for the Advancement of Science. No claim to original U.S. Government Works. Distributed under a Creative Commons Attribution NonCommercial License 4.0 (CC BY-NC).

Autism spectrum disorders (ASDs) are neurodevelopmental conditions characterized by social deficits, repetitive behaviors, and comorbidities such as sensory abnormalities, sleep disturbances, and seizures. Although thalamocortical circuit dysfunction has been implicated in these symptoms, its precise roles in ASD pathophysiology remain poorly understood. Here, we examine the specific contribution of the reticular thalamic nucleus (RT), a key modulator of thalamocortical activity, to ASD-related behavioral deficits using a *Cntnap2* knockout mouse model. *Cntnap2*$^{-/-}$ mice displayed increased seizure susceptibility, locomotor activity, and repetitive behaviors. Electrophysiological recordings revealed enhanced intrathalamic oscillations and burst firing in RT neurons, accompanied by elevated T-type calcium currents. In vivo fiber photometry confirmed behavior-associated increases in RT population activity. Notably, pharmacological and chemogenetic suppression of RT excitability via Z944, a T-type calcium channel blocker, and via C21 activation of the inhibitory DREADD hM4Di significantly improved ASD-related behaviors. These findings identify RT hyperexcitability as a mechanistic driver of ASD and highlight RT as a potential therapeutic target.

INTRODUCTION

Autism spectrum disorders (ASDs) are common neurodevelopmental conditions characterized by social impairments, repetitive behaviors, and comorbidities such as intellectual disability, hyperactivity, anxiety, and epilepsy. Extensive research has sought to unravel its pathophysiology by investigating cellular and circuit-level mechanisms across multiple brain regions, including the hippocampus, prefrontal cortex, and medial septum, through studies using various ASD-associated risk genes and animal models (*1*–*8*). Notably, individuals with ASD often exhibit sensory processing abnormalities (*9*, *10*), sleep disturbances (*11*, *12*), and seizures (*13*, *14*), implicating a potential role of the thalamocortical (TC) circuit, a key system governing these functions. Structural alterations in the thalamus and atypical TC connectivity have been reported in both juvenile and adult individuals with ASD (*15*–*17*). Recent findings further establish a link between electrophysiological abnormalities within the somatosensory thalamic nucleus and the sensory hypersensitivity and sleep fragmentation observed in children with ASD (*18*).

The reticular thalamic nucleus (RT) is a shell-like GABAergic nucleus that sends inhibitory projections exclusively to the thalamus, acting as the "gatekeeper" for sensory processing, fear, attention, and seizure regulation by modulating TC activity (*19*–*24*). RT neurons exhibit two distinct firing modes (*25*): burst and tonic firing. Burst firing, driven by T-type Ca^{2+} channels (*26*), generates high-frequency action potential (AP) trains that elicit strong inhibitory responses (*27*, *28*), followed by rebound burst (RB) firing in downstream TC neurons. At the network level, this interplay can trigger re-excitation of RT neurons, establishing a reciprocal RT-TC loop underlying intrinsic thalamic oscillations. As the principal source of intrathalamic inhibition, RT neurons coordinate key neural rhythms including sleep spindles, slow oscillations, and gamma oscillations (*29*–*32*). Disruptions in RT function perturb these dynamics and have been implicated in neuropsychiatric disorders such as attention-deficit/hyperactivity disorder (*33*), schizophrenia (*34*, *35*), and depressive-like behaviors (*36*). Although emerging data suggest that RT dysfunction contributes to ASD pathophysiology, the precise cellular and circuit-level mechanisms remain largely unexplored, warranting further investigation.

Contactin-associated protein–like 2 (Cntnap2) is strongly implicated in ASD, and *Cntnap2*$^{-/-}$ mice exhibit a range of ASD-related behaviors, including hyperactivity, epileptic seizures, disrupted sleep architecture, impaired sensory coding, and deficits in spatial discrimination (*1*, *4*, *37*–*39*). Previous studies have identified network, cellular, and structural alterations in these ASD model mice, including (i) altered hippocampal gamma oscillations and sharp wave ripples, accompanied by reduced parvalbumin-positive (PV^+) interneuron numbers and impaired perisomatic inhibition onto CA1 pyramidal cells (*37*, *40*); (ii) disturbed oscillatory population activity in the medial prefrontal cortex, with an altered excitation-to-inhibition balance in L2/3 pyramidal neurons and associated synaptic structures (*8*); and (iii) a transient reduction in dendritic spine density and increased microglial presynaptic engulfment in the anterior cingulate cortex (*41*). Here, we investigated electrophysiological changes in RT neurons in *Cntnap2*$^{-/-}$ mice and assessed their impact on ASD-relevant behaviors. Pharmacological and chemogenetic suppression of RT activity effectively ameliorated behavioral deficits, establishing a causal role for RT hyperexcitability in ASD pathophysiology. Our findings provide the evidence of RT hyperexcitability contributing to ASD-related behaviors and highlight the RT as a promising therapeutic target for managing ASD.

RESULTS

Elevated seizure susceptibility and locomotor activity in *Cntnap2*$^{-/-}$ mice

Previous studies have reported a comorbidity between ASD, hyperactivity, and a higher prevalence of seizures in both patients and

Department of Neurology and Neurological Sciences, Stanford University School of Medicine, Stanford, CA 94305, USA.
*Corresponding author. Email: john.huguenard@stanford.edu

Downloaded from https://www.science.org at Stanford University on August 25, 2025

animal models (*38*, *42*). To investigate whether *Cntnap2*$^{-/-}$ mice exhibit enhanced seizure susceptibility and locomotor activity, we primarily monitored cortical activity under electroencephalogram (EEG) recording following intraperitoneal administration of 20 mg/kg pentylenetetrazole (PTZ), a γ-aminobutyric acid type A (GABA$_A$) receptor antagonist, which at this low dose in mice generally is either subthreshold for evoking seizures or only produces mild, nonconvulsive seizures (*43*–*47*). Given the known variability in seizure susceptibility (*48*), we minimized the risk of false-negative results by testing equal numbers of wild-type (WT) and knockout (KO) animals on the same day under identical conditions. *Cntnap2*$^{-/-}$ mice exhibited a range of seizure phenotypes, including spike-wave discharges (SWDs) at 4 to 7 Hz, myoclonic jerks (MJs), generalized tonic-clonic seizures (GTCSs), and occasional mortality during the 10-min monitoring period (Fig. 1A). Seizure progression was common, especially in *Cntnap2*$^{-/-}$ mice, where initial SWDs were seen followed by MJs, then GTCSs, and sometimes death. We calculated final seizure scores and observed a significant increase in *Cntnap2*$^{-/-}$ mice compared to those in *Cntnap2*$^{+/+}$ mice (Fig. 1B), demonstrating heightened seizure susceptibility in *Cntnap2*$^{-/-}$ mice. Last, we also measured latency to both SWDs and MJs and found that *Cntnap2*$^{-/-}$ mice displayed significantly shorter latency to both SWDs (*Cntnap2*$^{+/+}$ mice: 9 of 11; *Cntnap2*$^{-/-}$ mice: 8 of 10) and MJs (*Cntnap2*$^{+/+}$ mice: 5 of 11; *Cntnap2*$^{-/-}$ mice: 8 of 10) compared to *Cntnap2*$^{+/+}$ controls (Fig. 1, C and D).

In addition to enhanced seizure propensity, *Cntnap2*$^{-/-}$ mice displayed increased locomotor activity, as evidenced by a greater total distance traveled in the open field during the 10-min session

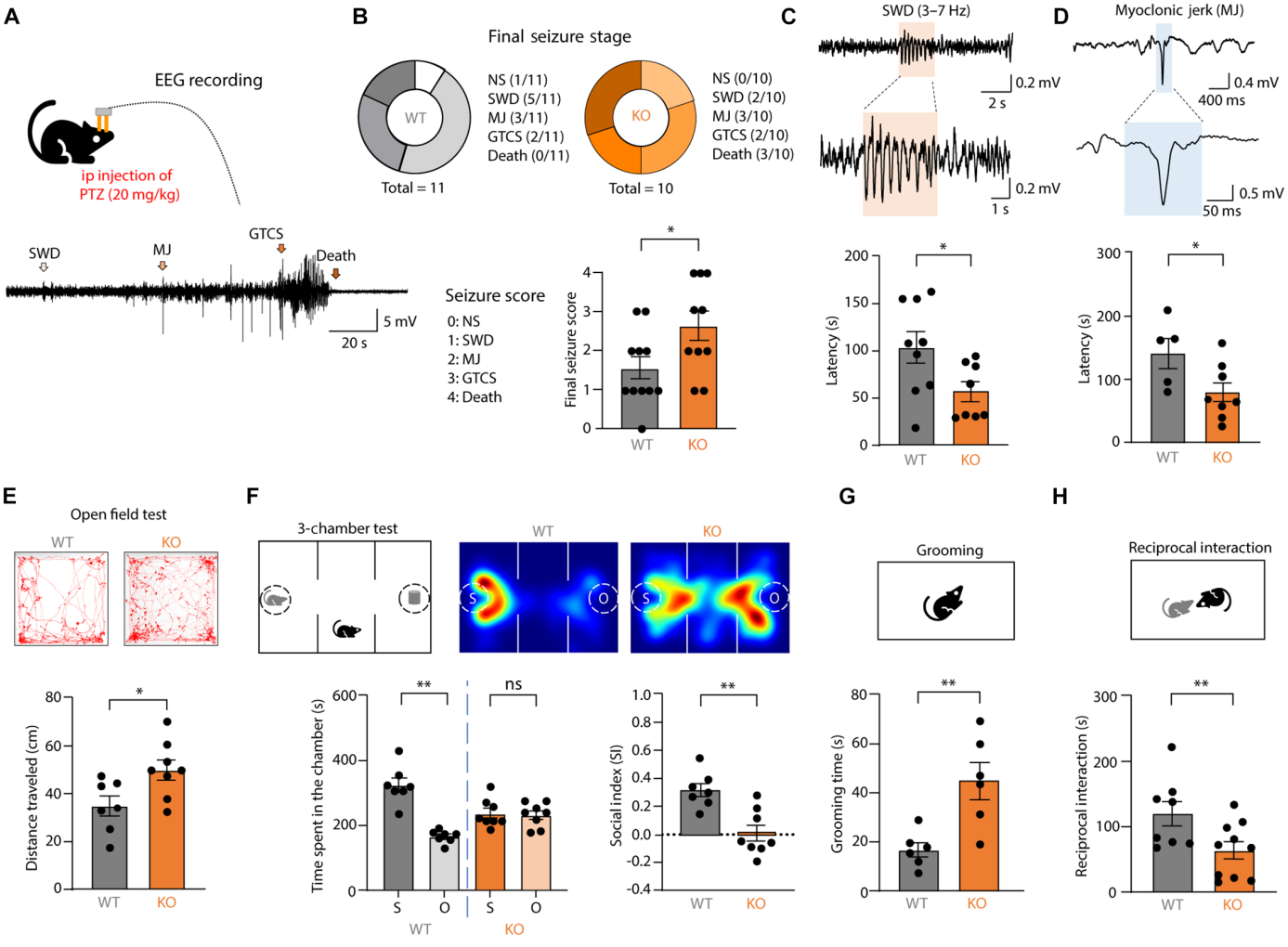


Fig. 1. *Cntnap2*$^{-/-}$ mice display increased seizure susceptibility, hyperactivity, and ASD-related behaviors. (**A**) Representative EEG trace showing epileptiform spike discharges, including SWD, MJ, GTCS, and death in *Cntnap2*$^{-/-}$ mice following intraperitoneal (ip) injection of PTZ (20 mg/kg). (**B**) Pie chart (top) illustrating distribution of mice by final seizure stages [0: nonseizure (NS); 1: SWD; 2: MJ; 3: GTCS; 4: death] and quantification (bottom) of the final seizure score in *Cntnap2*$^{+/+}$ and *Cntnap2*$^{-/-}$ mice. (**C** and **D**) Representative EEG traces (top) and quantification (bottom) of latency to first SWD (C) and MJ (D) (SWD: $n = 9$ for *Cntnap2*$^{+/+}$ and $n = 8$ for *Cntnap2*$^{-/-}$; MJ: $n = 5$ for *Cntnap2*$^{+/+}$ and $n = 8$ for *Cntnap2*$^{-/-}$). (**E**) Representative traces (top) showing position tracking in an open arena and quantification (bottom) of distance traveled over 10 min ($n = 7$ for *Cntnap2*$^{+/+}$ and $n = 8$ for *Cntnap2*$^{-/-}$). (**F**) Schematic (top, left) of three-chamber social preference test with heatmaps (top, right) of the topographical time distribution. Quantification (bottom) of time spent in the social (S) versus object (O) chamber and calculated social index ($n = 7$ for *Cntnap2*$^{+/+}$ and $n = 8$ for *Cntnap2*$^{-/-}$). (**G**) Schematic (top) of grooming behavioral assay and quantification (bottom) of grooming time for 10 min ($n = 6$ for *Cntnap2*$^{+/+}$ and $n = 6$ for *Cntnap2*$^{-/-}$). (**H**) Schematic (top) of reciprocal interaction and quantification (bottom) of reciprocal interaction time for 10 min ($n = 8$ for *Cntnap2*$^{+/+}$ and $n = 10$ for *Cntnap2*$^{-/-}$). The statistical tests involved an unpaired two-tailed *t* test (B to H). Data are presented as the mean values ± SEM. *P* values in figure panels: ns, not significant; $^*P < 0.05$; $^{**}P < 0.01$.

Downloaded from https://www.science.org at Stanford University on August 25, 2025

(Fig. 1E); showed little social preference, spending equal amounts of time in chambers containing a social partner (S) or an object (O) (Fig. 1F); and exhibited a reduced social index (Fig. 1F). Furthermore, *Cntnap2*$^{-/-}$ mice displayed elevated grooming behavior (Fig. 1G) and reduced reciprocal interaction time (Fig. 1H) during the 10-min test period, highlighting behavioral abnormalities associated with ASD. To further examine whether deficits in social preference are correlated with heightened seizure propensity and locomotor activity, we performed correlation analyses: (i) between the SWD latency and the social index and (ii) between the total distance traveled during the 10-min open-field test and the social index. Our analysis revealed that shorter SWD latency (fig. S1A) and greater locomotor activity (fig. S1B) were both correlated with reduced social preference. Collectively, these findings highlight a relationship between network hyperexcitability and core ASD-related behaviors in *Cntnap2*$^{-/-}$ mice, supporting their utility as a model for investigating ASD pathophysiology and comorbid features.

Thalamic circuit hyperexcitability in *Cntnap2*$^{-/-}$ mice

Given the relationship between TC dysfunction and behavioral deficits, including in Dravet syndrome mice (*49*), and absence seizures (*50*, *51*), we hypothesized that *Cntnap2*$^{-/-}$ mice may display impairment in TC rhythmicity. The TC loop involves reciprocal long-range connections between specific thalamic nuclei [e.g., ventrobasal thalamus (VB)] and corresponding cortical regions (e.g., primary somatosensory cortex), with each projection also sending collaterals to the GABAergic RT; these circuits together generate TC rhythms (Fig. 2, A and B). The intrathalamic network that supports these rhythms is maintained in horizontally sectioned brain slices (*50*–*53*), in which evoked oscillations can be triggered with extracellular stimuli applied to the internal capsule (i.c.). Spontaneously occurring oscillations can also be observed (*50*, *54*). In our extracellular recordings, slices from *Cntnap2*$^{-/-}$ mice displayed increased spontaneous oscillations including a higher incidence (6 of 10 slices in *Cntnap2*$^{-/-}$ compared to 0 of 9 slices in *Cntnap2*$^{+/+}$), with an increase in both total oscillation duration and number of bursts (Fig. 2C). In addition, evoked oscillations in response to electrical stimulation of the i.c. were enhanced in *Cntnap2*$^{-/-}$ mice, with increased oscillation duration and number of bursts per each stimulation, while oscillation frequency remained unchanged (Fig. 2D). To complement the results with electrical stimulation, we used *Cntnap2*$^{-/-}$ × Ai32 × Ntsr1-Cre mice expressing channelrhodopsin-2 (ChR2) in layer 6 corticothalamic (L6 CT) neurons projecting to thalamic nuclei, including VB and RT (Fig. 2E), and successfully confirmed evoked oscillations via a short optogenetic stimulation (3 mW/mm^2, 1 ms) (Fig. 2E). Similar to results with electrical i.c. stimulation, optogenetic stimulation in slices from *Cntnap2*$^{-/-}$ mice resulted in the increased duration of oscillation and number of bursts per each stimulation without affecting oscillation frequency (Fig. 2E). Together, these findings reveal increased spontaneous and evoked intrathalamic oscillations in *Cntnap2*$^{-/-}$ mice, which may contribute to the pathophysiology underlying ASD-related deficits.

Increased burst firing in the RT of *Cntnap2*$^{-/-}$ mice

RT neurons, most of which express PV (*55*), provide the primary inhibitory input to TC circuits and play a critical role in regulating distinct types of oscillatory activity (*56*). Previous studies have shown that the dysfunction or altered expression of PV in PV-expressing GABAergic interneurons renders them highly susceptible to ASD-related factors (*57*, *58*), contributing to deficits such as impaired sensory gating and disruption of the excitation/inhibition balance in the cortex and hippocampus (*59*, *60*). To determine whether electrophysiological properties of RT neurons, which are known to highly express PV, are altered in *Cntnap2*$^{-/-}$ mice, we recorded both passive and active membrane properties from RT neurons in acute horizontal brain slices (Fig. 3A). We observed no differences in passive membrane properties including membrane capacitance (pF), resting membrane potential, and input resistance between *Cntnap2*$^{+/+}$ and *Cntnap2*$^{-/-}$ mice (fig. S2, A to C). However, the number of APs elicited by depolarizing current injection was significantly increased (Fig. 3B), with reduced rheobase (Fig. 3C). RT responses at rest consisted of an early burst firing phase, complete within 100 ms, and a later tonic firing phase (*61*). The number of spikes evoked during the first bursting phase was increased in *Cntnap2*$^{-/-}$ mice, but those during the tonic phase were unaffected (Fig. 3D). No significant changes were observed in individual AP properties, including fast afterhyperpolarization, AP threshold, half-width, spike height, maximum dV/dt, or minimum dV/dt of the first and last spikes elicited by a 210-pA injection (fig. S2, D to O). RT neurons fire multiple RBs at the termination of hyperpolarizing steps (*25*, *49*, *62*, *63*). We recorded RBs elicited from a range of holding potentials between −70 and −50 mV. Unexpectedly, at −70 mV, some of the RT neurons (7 of 18) in *Cntnap2*$^{-/-}$ mice produced RBs, whereas none of those (0 of 18) in *Cntnap2*$^{+/+}$ mice did. At −60 mV, most of the RT neurons (15 of 18) in *Cntnap2*$^{-/-}$ neurons generated RBs compared to about half of the RT neurons (9 of 18) in *Cntnap2*$^{+/+}$ neurons (Fig. 3E). In addition, the number of rebound oscillatory bursts elicited by different holding potentials (−70 to −50 mV) was increased in *Cntnap2*$^{-/-}$ neurons (Fig. 3F), with no change in the number of spikes in the first RB elicited under −55- and −50-mV holding potentials (Fig. 3G). Given the critical role of low-threshold T-type calcium channels in generating RB firing, we assessed T-type calcium currents using a steady-state inactivation protocol (*26*), applying hyperpolarizing prepulses (−105 to −65 mV) followed by a test pulse to −55 mV, with consistent peak latencies indicating reliable voltage clamp control (as indicated by the black dashed line in the traces) (Fig. 3H). For the final analysis, we only included responses from RT neurons that exhibited consistent peak latencies and then normalized peak amplitudes to membrane capacitance to calculate the current density. Using this approach, we found that *Cntnap2*$^{-/-}$ RT neurons exhibited significantly increased inward current density (Fig. 3H). To assess whether synaptic inputs to RT are also altered in *Cntnap2*$^{-/-}$ mice, we recorded spontaneous excitatory postsynaptic currents (sEPSCs) and spontaneous inhibitory postsynaptic currents (sIPSCs) in RT neurons and found no significant differences in the frequency, amplitude, rise time, and half-width of sEPSCs and sIPSCs between genotypes (fig. S3, A and B). Together, these results indicate that *Cntnap2*$^{-/-}$ RT neurons exhibit increased intrinsic burst firing, presumably driven by enhanced T-type calcium channel function, which may contribute to elevated TC circuit oscillations and ASD-related circuit dysfunction.

Altered inhibitory output to TC in *Cntnap2*$^{-/-}$ mice

Elevation of intrinsic excitability in RT neurons of *Cntnap2*$^{-/-}$ mice is predicted to strengthen RT synaptic outputs to TC neurons. To investigate this, we recorded sIPSCs in TC neurons within the VB nuclei. Our results revealed a significant increase in sIPSC frequency,

Downloaded from https://www.science.org at Stanford University on August 25, 2025

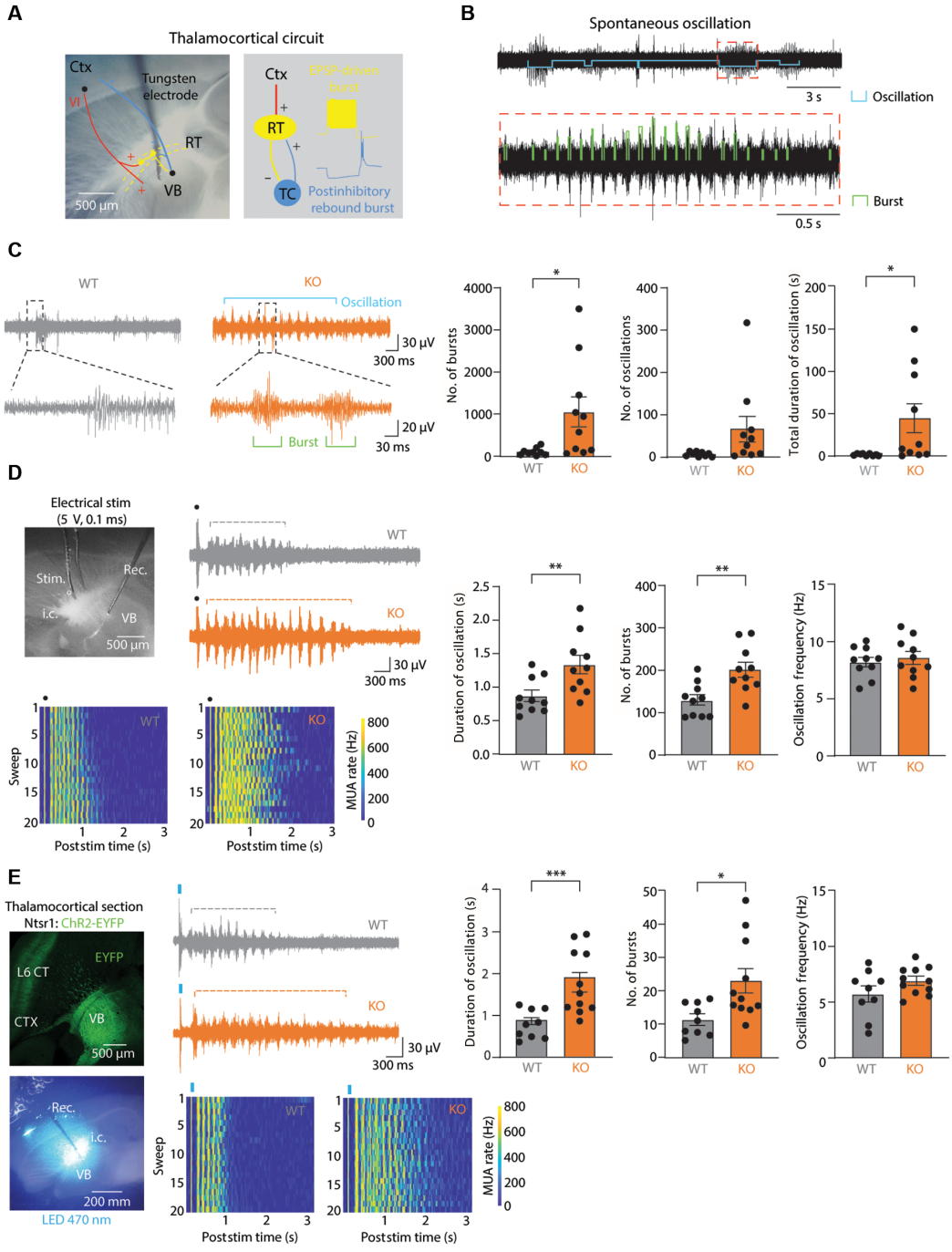


Fig. 2. The intrathalamic circuit is hyperexcitable in *Cntnap2*$^{-/-}$ mice. (**A**) Schematic (left) depicting the TC circuit showing corticothalamic (red), TC (blue), and reticular thalamic (yellow) projections and membrane potential traces (right) of RT and TC cells during thalamic oscillation. (**B**) Representative traces showing spontaneous oscillations (downward blue bracket) composed of many individual bursts of APs (upward green brackets). (**C**) Representative traces (left) of spontaneous oscillation and quantification (right) of the number of burst, the number of oscillations, and total duration of oscillation ($n = 9$ for *Cntnap2*$^{+/+}$ and $n = 10$ for *Cntnap2*$^{-/-}$). (**D**) Representative image (top, left) of evoked oscillation recording with electrical stimulation wires in the i.c. and a recording electrode (Rec.) in VB, representative traces (top, right) of evoked oscillation, heatmaps (bottom) showing representative peristimulus time histograms for detected spikes over 20 sequentially evoked responses, and quantification (right) of duration of oscillation, the number of bursts, and oscillation frequency ($n = 10$ for *Cntnap2*$^{+/+}$ and $n = 10$ for *Cntnap2*$^{-/-}$). Color intensity codes the number of spikes in each time bin. (**E**) Representative image (top, left) showing EYFP expression in Ai32-Ntsr1-ChR2-EYFP mice, representative image (bottom, left) showing the location illuminated by the 470-nm laser, representative traces (top, right) showing evoked oscillations, heatmaps (bottom, right) showing representative peristimulus time histograms, and quantification (right) of duration of oscillation, the number of bursts, and oscillation frequency ($n = 9$ for *Cntnap2*$^{+/+}$ and $n = 11$ for *Cntnap2*$^{-/-}$). MUA, multiunit activity. The statistical tests involved an unpaired two-tailed *t* test (C to E), confirmed by performing a mixed-effects model (REML). Data are presented as the mean values ± SEM. *P* values in figure panels: $^{*}P < 0.05$; $^{**}P < 0.01$; $^{***}P < 0.001$.

Downloaded from https://www.science.org at Stanford University on August 25, 2025

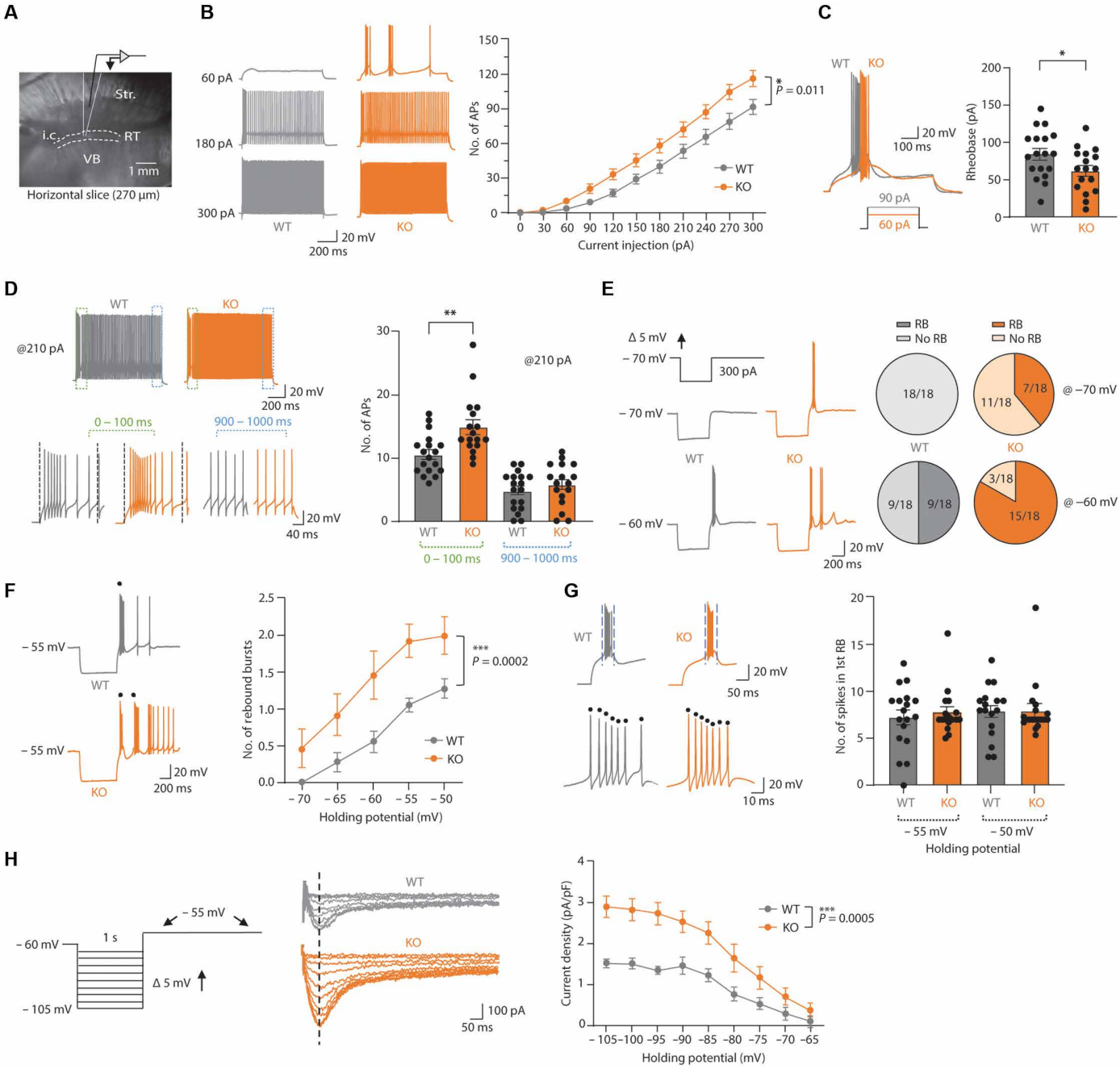


Fig. 3. Elevated burst firing in the RT neuron underlies increased intrinsic excitability in *Cntnap2*$^{-/-}$ mice. (**A**) Bright-field image depicting whole-cell patch-clamp recording of RT neuron in horizontal thalamic slice. (**B**) Representative traces (left) showing APs elicited by current injection and quantification (right) of the number of APs elicited by 0- to 300-pA injection. (**C**) Representative traces (left) showing burst firing elicited by injecting rheobase current and quantification (right) of rheobase current. (**D**) Representative traces (left) showing APs containing an initial burst (first 0 to 100 ms) and tonic firing (last 900 to 1000 ms) elicited by injecting 210 pA and quantification (right) of the number of APs during an initial burst and tonic firing. (**E**) Representative traces (left) showing RBs elicited by hyperpolarizing current and pie charts (right) illustrating the proportion of cells producing RBs at holding potentials of −70 and −60 mV. (**F**) Representative traces (left) showing oscillatory RBs and quantification (right) of the number of RB firing. Black dots indicate single burst. (**G**) Representative traces (left) showing RB spikes and quantification (right) of the number of spikes. Black dots indicate individual spikes. (**H**) Protocol and representative traces (left) showing T-type Ca^{2+}currents and quantification (right) of current density (pA/pF) of T-type Ca^{2+}currents. Dashed lines indicate constant peak latencies. (B to G) $n = 18$ for *Cntnap2*$^{+/+}$ and $n = 17$ for *Cntnap2*$^{-/-}$. (H) $n = 15$ for *Cntnap2*$^{+/+}$ and $n = 14$ for *Cntnap2*$^{-/-}$ The statistical tests involved a two-way ANOVA (B, F, and H) followed by multiple comparisons using Tukey's post hoc test and an unpaired two-tailed *t* test (C and D), confirmed by performing a mixed-effects model (REML). Data are presented as the mean values ± SEM. *P* values in figure panels: $*P < 0.05$; $**P < 0.01$; $***P < 0.001$.

Downloaded from https://www.science.org at Stanford University on August 25, 2025

while the amplitude, rise time, and half-width remained unchanged (Fig. 4A), suggesting an increase in the spontaneous presynaptic excitability of RT neurons in *Cntnap2*$^{-/-}$ mice. To further assess presynaptic activity, AAV2-DIO-hChR2-EYFP was infused into RT of *Cntnap2*$^{+/+}$ × PV-Cre and *Cntnap2*$^{-/-}$ × PV-Cre mice in which behavioral deficits were successfully confirmed (fig. S4), and the expression of hChR2 was confirmed by enhanced yellow fluorescent protein (EYFP)–labeled RT neurons and their axon terminals (Fig. 4B). Blue light stimulation (1 ms, 470 nm) effectively evoked inhibitory postsynaptic currents (eIPSCs) in TC neurons held at −70 mV (Fig. 4C). These eIPSCs were confirmed to be $GABA_A$ receptor–dependent chloride currents using two approaches: (i) recording at different holding potentials [−70 mV; +5 mV, the estimated chloride (Cl^-) reversal potential; and +35 mV] and (ii) applying SR-95531, a $GABA_A$ receptor antagonist (Fig. 4C). After confirming reliable eIPSCs in TC neurons with optogenetic stimulation, we assessed presynaptic release dynamics by measuring (i) the paired-pulse ratio (PPR), a marker of presynaptic release probability, and (ii) the synaptic failure rate, a readout for synaptic fidelity. Our optogenetic recording revealed a significant increase in the PPR at 50- and 100-ms intervals in *Cntnap2*$^{-/-}$ mice, indicating alterations in the presynaptic properties of RT inputs onto TC neurons (Fig. 4D). However, we did not see any differences in failure rate at a range of stimulation from 2 to 30 Hz (Fig. 4E). These findings demonstrate that *Cntnap2*$^{-/-}$ mice display altered synaptic features at the RT-TC synapses, including (i) elevated spontaneous presynaptic excitability and (ii) presynaptic change in release from RT terminals onto TC cells, which may also contribute to TC circuit dysfunction in *Cntnap2*$^{-/-}$ mice.

Elevated behavior-related RT activity in *Cntnap2*$^{-/-}$ mice

A recent study using in vivo fiber photometry has demonstrated spontaneous Ca^{2+} transients in RT neurons (*64*), reflecting neuronal activity. Given our findings of increased intrinsic burst firing and presynaptic activity of RT neurons in *Cntnap2*$^{-/-}$ mice, we hypothesized that in vivo RT population activity would be elevated and would show distinct responses to external stimuli, including light, social interaction, inanimate objects, and mild seizures in *Cntnap2*$^{-/-}$ mice. To test this, we injected AAV2/9-EF1a-DIO-GCaMP6f into RT regions of *Cntnap2*$^{+/+}$ × PV-Cre and *Cntnap2*$^{-/-}$ × PV-Cre mice (Fig. 5A). Four weeks post–adeno-associated virus (AAV) injection,

Downloaded from https://www.science.org at Stanford University on August 25, 2025

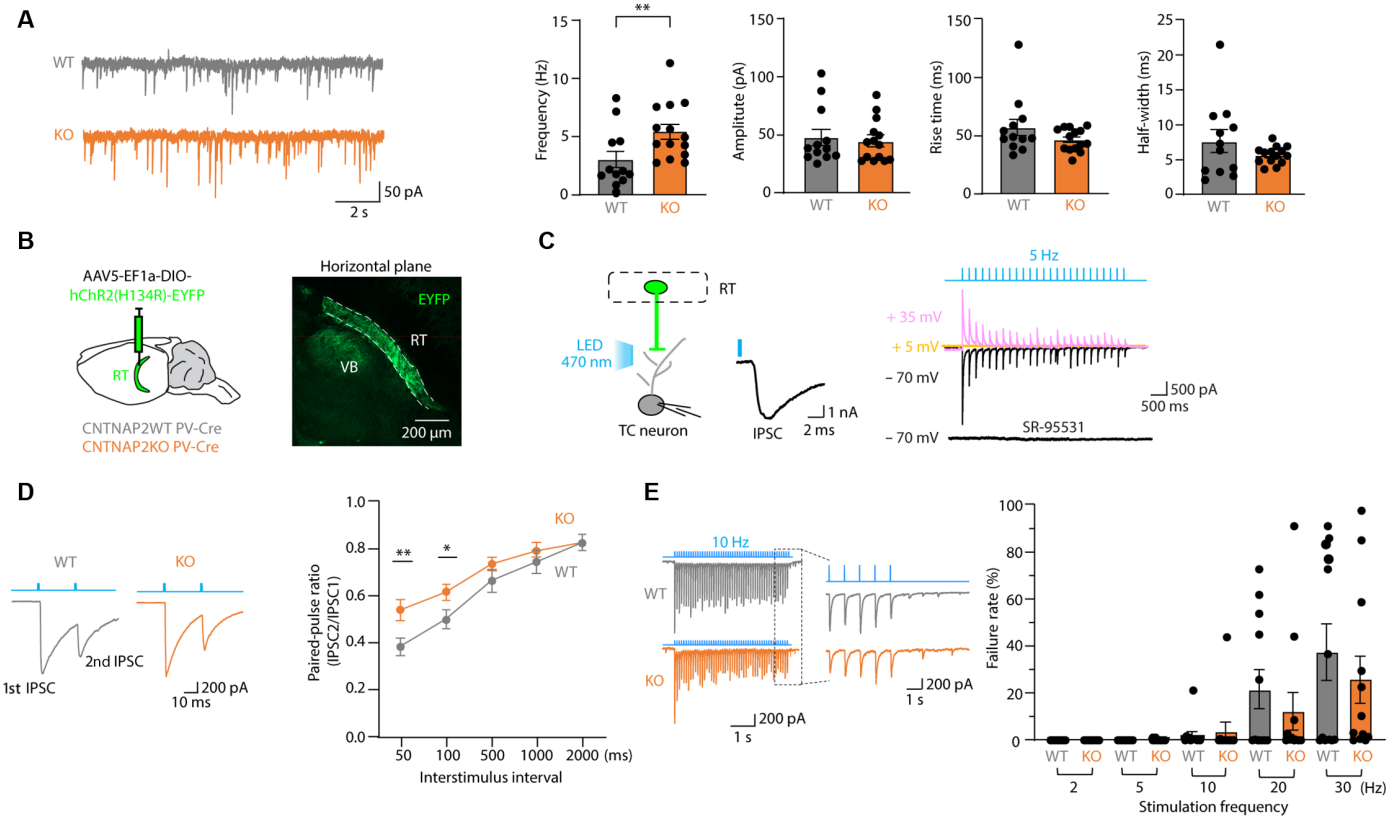


Fig. 4. Synaptic inhibitory output from RT → TC is altered in *Cntnap2*$^{-/-}$ mice. (**A**) Representative traces (left) showing spontaneous IPSCs and quantification (right) of the IPSC frequency (Hz), amplitude (pA), rise time (ms), and half-width (ms) ($n = 12$ for *Cntnap2*$^{+/+}$ and $n = 14$ for *Cntnap2*$^{-/-}$). (**B**) Schematic (left) describing stereotaxic injection of AAV5-EF1a-DIO-hChR2(H134R)-EYFP into the RT region and green fluorescence (right) representing the expression of EYFP in the RT. (**C**) Schematic (left) describing the experimental strategy and a single IPSC (left) elicited by optogenetic stimulation to the RT expressing ChR2 and characterization (right) of IPSCs elicited by different membrane holding potentials (−70, −5, and +35 mV) and drug treatment with SR-95531. (**D**) Representative traces (left) showing IPSCs elicited by paired pulses with different interstimulus intervals (50, 100, 500, 1000, and 2000 ms) and quantification (right) of PPR ($n = 13$ for *Cntnap2*$^{+/+}$ and $n = 11$ for *Cntnap2*$^{-/-}$). (**E**) Representative traces (left) showing IPSCs elicited by 5-s-long stimulations at different stimulation frequencies (2, 5, 10, 20, and 30 Hz) and quantification (right) of failure rate ($n = 12$ for *Cntnap2*$^{+/+}$ and $n = 12$ for *Cntnap2*$^{-/-}$). The statistical tests involved an unpaired two-tailed *t* test (A, D, and E), confirmed by performing a mixed-effects model (REML). Data are presented as the mean values ± SEM. *P* values in figure panels: $*P < 0.05$; $**P < 0.01$.

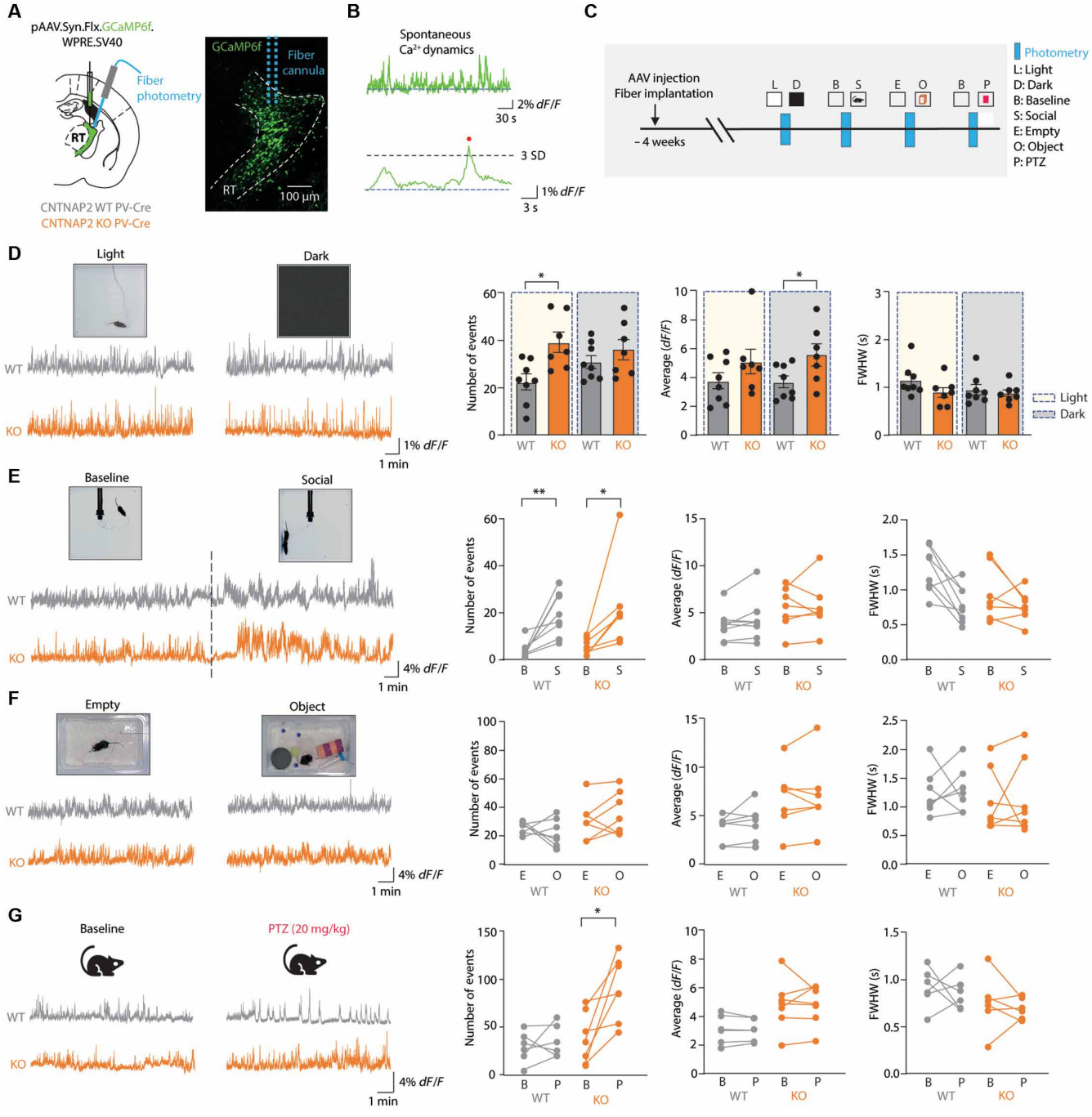


Fig. 5. The in vivo RT population activity is elevated in *Cntnap2*$^{-/-}$ mice. (**A**) Schematic (left) describing stereotaxic injection and fiber cannula implantation into the RT region and green fluorescence (right) representing GCaMP6f expression. (**B**) Representative trace (top) showing spontaneous Ca^{2+} dynamics and detection criteria (bottom). The red dot indicates the event. (**C**) Schematic illustrating experimental conditions and strategy to measure spontaneous Ca^{2+} dynamics. (**D**) Representative images (top, left) showing experimental conditions, representative traces (bottom, left) of spontaneous Ca^{2+} dynamics during light and dark conditions, and quantification (right) of the number of events, average *dF/F*, and FWHM of Ca^{2+} dynamics ($n = 8$ for *Cntnap2*$^{+/+}$ and $n = 7$ for *Cntnap2*$^{-/-}$). (**E**) Representative images (top, left) experimental conditions, representative traces (bottom, left) of spontaneous Ca^{2+} dynamics during the baseline and social interaction, and quantification (right) of the number of events, average *dF/F*, and FWHM in Ca^{2+} dynamics ($n = 8$ for *Cntnap2*$^{+/+}$ and $n = 7$ for *Cntnap2*$^{-/-}$). (**F**) Representative images (top, left) showing experimental conditions and representative traces (bottom, left) of spontaneous Ca^{2+} dynamics during empty and object conditions and quantification (right) of the number of events, average *dF/F*, and FWHM in Ca^{2+} dynamics ($n = 7$ for *Cntnap2*$^{+/+}$ and $n = 7$ for *Cntnap2*$^{-/-}$). (**G**) Schematic showing experimental conditions (top, left), representative traces (bottom, left) of spontaneous Ca^{2+} levels during the baseline and PTZ condition, and quantification (right) of the number of events, average *dF/F*, and FWHM in Ca^{2+} dynamics ($n = 6$ for *Cntnap2*$^{+/+}$ and $n = 6$ for *Cntnap2*$^{-/-}$). The statistical tests involved a two-way ANOVA with Tukey's test (D) and a paired two-tailed *t* test (E to G), confirmed by performing a mixed-effects model (REML). Data are presented as the mean values ± SEM. *P* values in figure panels: $*P < 0.05$; $**P < 0.01$.

Downloaded from https://www.science.org at Stanford University on August 25, 2025

the expression of GCaMP6f was confirmed by green fluorescence in the soma of RT neurons (Fig. 5A). Spontaneous calcium transients were reliably detected and quantified using a threshold of higher than 3 SDs above the baseline (Fig. 5B). We first assessed in vivo RT population activity under light and dark conditions, followed by recordings during social interactions, object exploration, and chemically induced seizures, with 3- to 5-day intervals between conditions to minimize confounding effects (Fig. 5C). Under light conditions, *Cntnap2*$^{-/-}$ mice showed a significant increase in the number of Ca^{2+} events, whereas no difference in event number was observed in the dark; however, the average event amplitude ($\Delta F/F$) was elevated in *Cntnap2*$^{-/-}$ mice under dark conditions (Fig. 5D). Consistent with the previous report (*65*), during social interaction, both genotypes displayed an increased number of events, but *Cntnap2*$^{+/+}$ mice showed a reduction in event full width at half maximum (FWHM) (Fig. 5E). In contrast, inanimate object exposure did not induce any changes in the number of events, the average event amplitude, and FWHM across genotypes (Fig. 5F). In response to air puff and tail pinch stimuli, the event amplitude was greater in *Cntnap2*$^{-/-}$ mice than in *Cntnap2*$^{+/+}$ mice (fig. S5, A and B). Last, consistent with increased seizure activity following PTZ injection (Fig. 1, A to C), *Cntnap2*$^{-/-}$ mice exhibited an increased number of events, an effect that was not observed in *Cntnap2*$^{+/+}$ mice (Fig. 5G). These results demonstrate that RT neurons in *Cntnap2*$^{-/-}$ mice exhibit altered spontaneous and stimulus-evoked population activity, suggesting that heightened in vivo RT population activity may contribute to ASD-related behavioral deficits.

Acute systemic inhibition of the T-type calcium channel restores behavioral deficits in *Cntnap2*$^{-/-}$ mice

Given the correlation between behavioral deficits and elevated burst firing and T-type calcium current density in RT neurons of *Cntnap2*$^{-/-}$ mice (Fig. 3, E to G), we hypothesized that inhibiting T-type calcium channels could rescue behavioral abnormalities observed in *Cntnap2*$^{-/-}$ mice. Before conducting behavioral rescue experiments, we validated the efficacy of Z944, a selective T-type calcium channel blocker (*66*), in suppressing (i) RT activity using both in vivo fiber photometry and whole-cell patch-clamp recording and (ii) seizure susceptibility via EEG monitoring. Systemic administration of Z944 (10 mg/kg) significantly reduced the number of events without affecting the average event amplitude and FWHM (fig. S6A) and increased latency to SWDs (fig. S6B) in both genotypes. In addition, in vitro bath application of Z944 (1 μM) significantly increased burst rheobase in both genotypes and normalized the reduced burst rheobase in *Cntnap2*$^{-/-}$ mice to levels comparable to those of *Cntnap2*$^{+/+}$ mice (fig. S6C). Consistent with this finding, Z944 also reversed the increased number of APs elicited by a 90-pA injection in *Cntnap2*$^{-/-}$ mice (fig. S6D). These findings confirm that Z944 effectively suppresses RT activity by inhibiting burst firing, thus supporting its use in subsequent behavioral rescue experiments. Behavioral assays were conducted at a 3- to 5-day interval between vehicle and Z944 conditions to allow recovery and avoid confounding effects of repeated behavioral tests. Each animal received either vehicle or Z944, not both, and treatment conditions were alternated across independent cohorts (Fig. 6A). In the open-field test, during the 10-min habituation phase, *Cntnap2*$^{-/-}$ mice displayed hyperlocomotor activity compared to *Cntnap2*$^{+/+}$ mice, which was normalized by Z944 (fig. S7A). During the subsequent 20-min test session, Z944 reduced hyperlocomotor activity in *Cntnap2*$^{-/-}$ mice, with no effect in *Cntnap2*$^{+/+}$ mice (Fig. 6B). In the three-chamber test, vehicle-treated *Cntnap2*$^{+/+}$ mice displayed a robust preference for the social partner, while *Cntnap2*$^{-/-}$ mice did not (Fig. 6C), replicating baseline deficits (Fig. 1E). Notably, Z944 restored social preference in *Cntnap2*$^{-/-}$ mice (Fig. 6C), consistent with manually scored sniffing time (fig. S7B). Z944 also reduced excessive grooming in *Cntnap2*$^{-/-}$ mice to control levels (Fig. 6D) without altering the number of grooming bouts (Fig. 6E) and digging time (Fig. 6F). In the reciprocal interaction test, Z944 rescued social interaction time in *Cntnap2*$^{-/-}$ mice (Fig. 6G), although it unexpectedly decreased the interaction time in *Cntnap2*$^{+/+}$ mice as well. Together, these findings highlight the therapeutic potential of targeting RT hyperexcitability through T-type calcium channel inhibition to alleviate core behavioral abnormalities in ASD.

Acute DREADD-mediated inhibition of RT restores behavioral deficits in *Cntnap2*$^{-/-}$ mice

Last, to test whether target-specific suppression of RT activity could mitigate behavioral deficits in *Cntnap2*$^{-/-}$ mice, we injected pAAV-hSyn-DIO-hM4D(Gi)-mCherry bilaterally into the RT of *Cntnap2*$^{+/+}$ mice × PV-Cre and *Cntnap2*$^{-/-}$ mice × PV-Cre mice. Four weeks post–AAV injection, the expression of mCherry was confirmed by red fluorescence in RT regions without spillover (Fig. 7A). In vitro whole-cell patch-clamp recordings in slices confirmed that bath application of C21 (5 μM) induced membrane hyperpolarization, reduced spontaneous APs (Fig. 7B), and increased rheobase in RT neurons (Fig. 7C), confirming that C21 effectively inhibits the excitability of RT neurons, thereby justifying its use in behavioral rescue experiments. As with the Z944 experiment, behavioral assays were conducted at a 3- to 5-day interval between vehicle and C21 conditions to allow for recovery and avoid confounding effects of repeated behavioral tests. Each animal received either vehicle or C21, not both, and treatment conditions were alternated across independent cohorts (Fig. 7D). In the open-field test, *Cntnap2*$^{-/-}$ mice exhibited hyperlocomotor activity during the 10-min habituation phase, which was unaffected by C21 injection (fig. S7C). However, during the 20-min test session, C21 significantly attenuated hyperactivity in *Cntnap2*$^{-/-}$ mice, reducing the total distance traveled to near levels of *Cntnap2*$^{+/+}$ mice, while *Cntnap2*$^{+/+}$ mice remained unaffected by treatment (Fig. 7E). In the three-chamber test, vehicle-treated *Cntnap2*$^{-/-}$ mice failed to show a preference for the social chamber, whereas C21 restored social preference in *Cntnap2*$^{-/-}$ mice (Fig. 7F) without affecting the total social sniffing time (fig. S7D). In the grooming test, C21 increased grooming time in *Cntnap2*$^{+/+}$ mice (Fig. 7G) and the number of grooming events (Fig. 7H), suggesting a role for RT in regulating repetitive behaviors. Notably, C21 rescued grooming time but not the number of grooming events in *Cntnap2*$^{-/-}$ mice (Fig. 7, G and H) without affecting digging behavior (Fig. 7I). In the reciprocal interaction test, C21 failed to rescue reciprocal social interaction observed in *Cntnap2*$^{-/-}$ mice (Fig. 7J). Last, to test whether increased RT activity is sufficient to induce ASD-like behaviors, we expressed hM3Dq-mCherry selectively in the RT with minimal off-target expression (fig. S8A) by bilaterally infusing pAAV-hSyn-DIO-hM3D(Gq)-mCherry into *Cntnap2*$^{+/+}$ × PV-Cre mice. Four weeks post–AAV injection, we confirmed the selective expression of hM3Dq-mCherry in RT regions with minimal off-target expression (fig. S8A). Bath application of C21 (5 μM) induced membrane depolarization in RT neurons, triggered spontaneous APs (fig. S8B), and reduced rheobase (fig. S8C), confirming

Downloaded from https://www.science.org at Stanford University on August 25, 2025

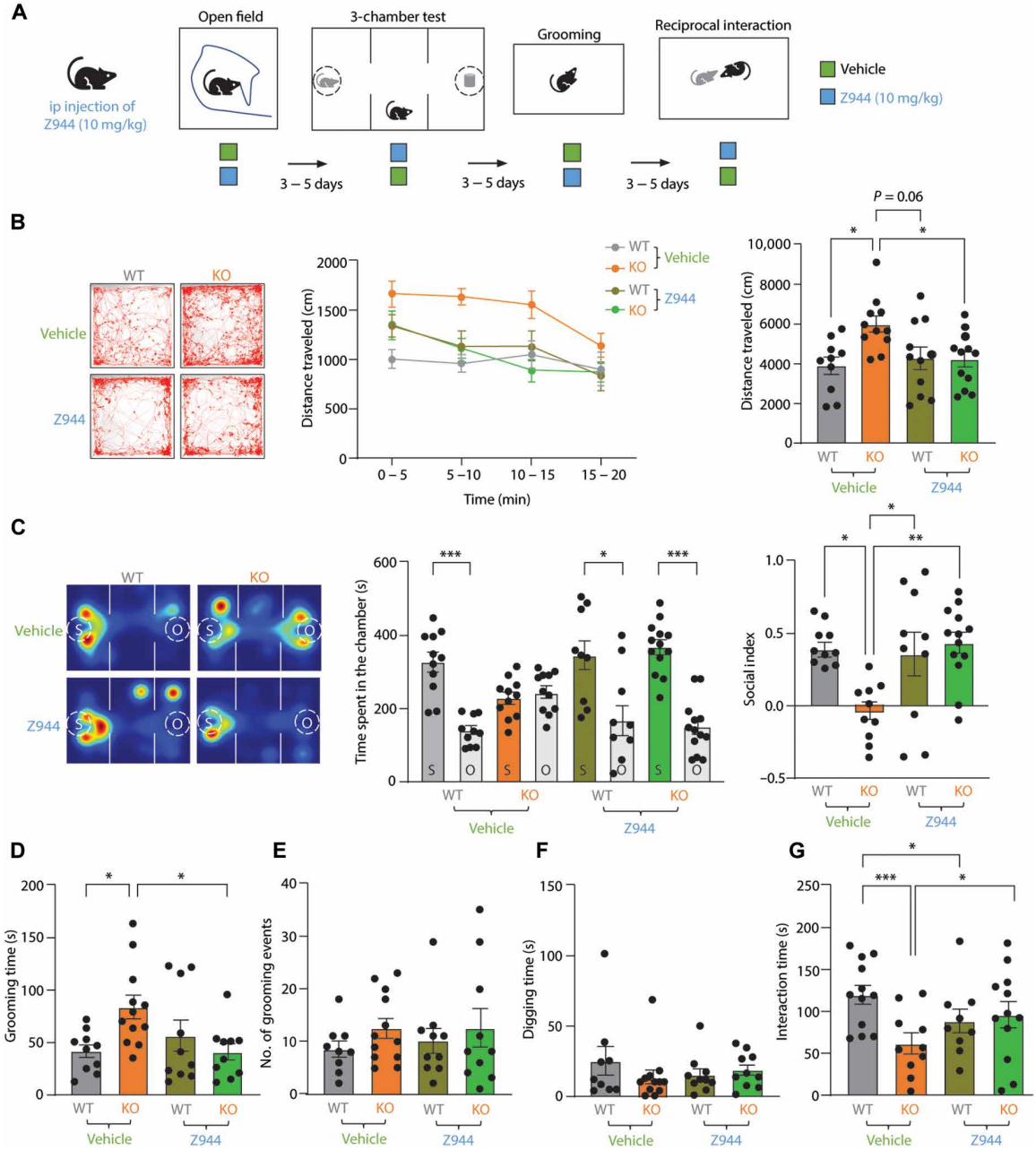


Fig. 6. Pharmacological inhibition of T-type calcium channels ameliorates ASD-related behaviors. (**A**) Schematic of experimental design for evaluating the rescue effect of Z944 (10 mg/kg), a T-type calcium channel inhibitor, on behavioral phenotypes. (**B**) Representative open field movement traces (left) and quantification of distance traveled (middle) in 5-min intervals and total distance (right) traveled over 20 min with vehicle or Z944 ($n = 10$ for *Cntnap2*$^{+/+}$-Veh, $n = 11$ for *Cntnap2*$^{-/-}$-Veh, $n = 11$ for *Cntnap2*$^{+/+}$-Z944, and $n = 12$ for *Cntnap2*$^{-/-}$-Z944). (**C**) Representative heatmaps (left) showing location density across time during the social preference test and quantification of time spent in each chamber (middle) and the social index (right) with vehicle or Z944 ($n = 11$ for *Cntnap2*$^{+/+}$-Veh, $n = 11$ for *Cntnap2*$^{-/-}$-Veh, $n = 10$ for *Cntnap2*$^{+/+}$-Z944, and $n = 13$ for *Cntnap2*$^{-/-}$-Z944). (**D** to **F**) Quantification of grooming time (D), the number of grooming events (E), and digging time (F) with vehicle or Z944 ($n = 10$ for *Cntnap2*$^{+/+}$-Veh, $n = 12$ for *Cntnap2*$^{-/-}$-Veh, $n = 10$ for *Cntnap2*$^{+/+}$-Z944, and $n = 10$ for *Cntnap2*$^{-/-}$-Z944). (**G**) Quantification of interaction time with vehicle or Z944 ($n = 12$ for *Cntnap2*$^{+/+}$-Veh, $n = 10$ for *Cntnap2*$^{-/-}$-Veh, $n = 9$ for *Cntnap2*$^{+/+}$-Z944, and $n = 12$ for *Cntnap2*$^{-/-}$-Z944). The statistical tests involved a two-way ANOVA with Tukey's test (B to D). Data are presented as the mean values ± SEM. *P* values in figure panels: $*P < 0.05$; $**P < 0.01$; $***P < 0.001$.

Downloaded from https://www.science.org at Stanford University on August 25, 2025

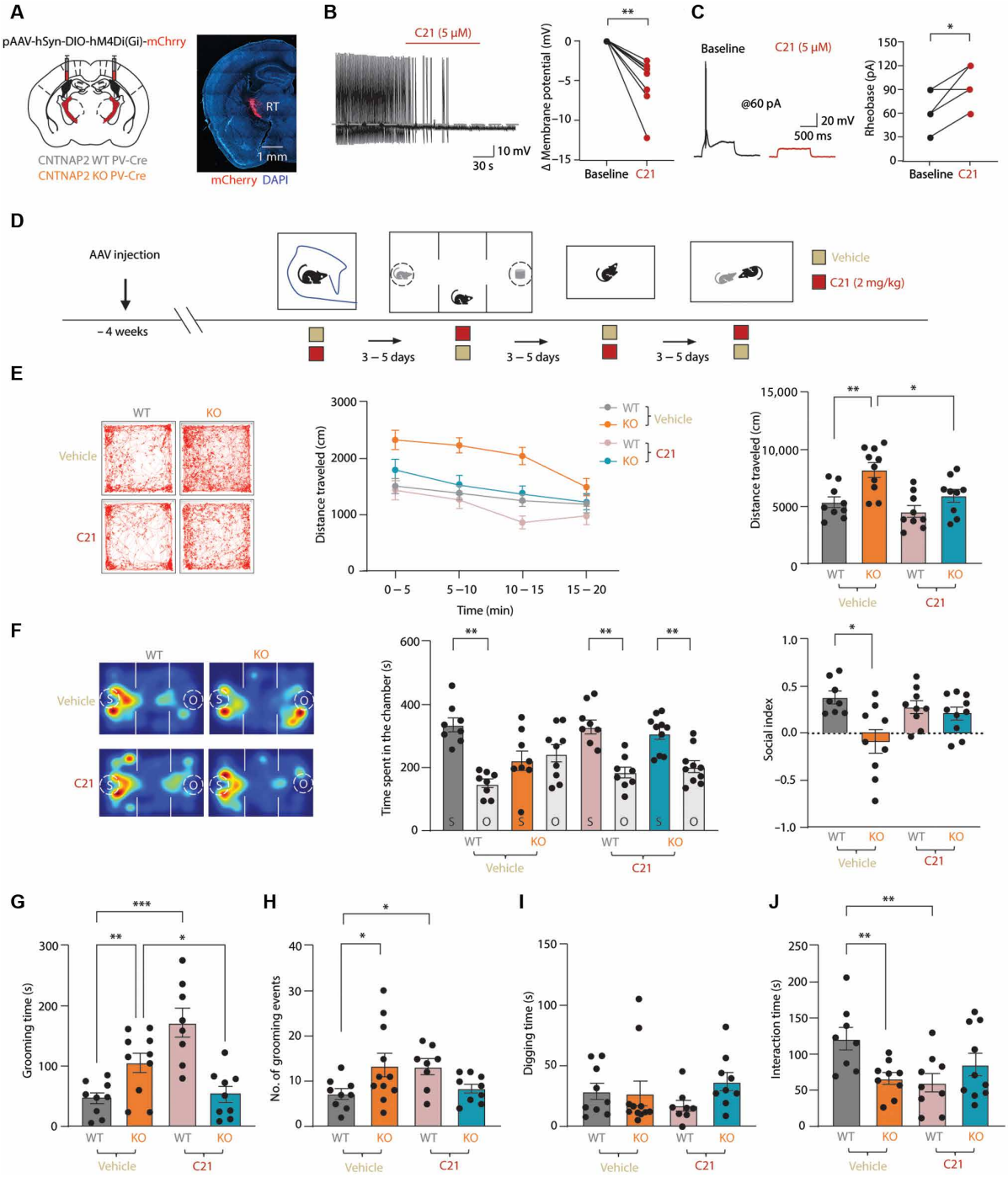


Fig. 7. Chemogenetic inhibition of RT ameliorates ASD-related behaviors. (**A**) Schematic (left) describing stereotaxic virus injection into the RT and red fluorescence (right) representing the expression of hM4D(Gi)-mCherry. DAPI, 4′,6-diamidino-2-phenylindole. (**B**) Representative trace (left) and quantification (right) of changes in membrane potential following bath application of C21 ($n = 7$). (**C**) Representative traces (left) showing APs elicited by rheobase currents and quantification (right) of C21-induced changes in rheobase ($n = 9$). (**D**) Experimental strategy for evaluating the rescue effect of chemogenetic inhibition on behavioral phenotypes. (**E**) Representative open field movement traces (left) and quantification of distance traveled in 5-min intervals (middle) and total distance traveled (right) over 20 min with vehicle or C21 ($n = 9$ for *Cntnap2*$^{+/+}$-Veh, $n = 10$ for *Cntnap2*$^{-/-}$-Veh, $n = 9$ for *Cntnap2*$^{+/+}$-C21, and $n = 9$ for *Cntnap2*$^{-/-}$-C21). (**F**) Representative heatmaps (left) showing location data during social preference tests and quantification of time spent in each chamber (middle) and the social index (right) with vehicle or C21 ($n = 8$ for *Cntnap2*$^{+/+}$-Veh, $n = 9$ for *Cntnap2*$^{-/-}$-Veh, $n = 9$ for *Cntnap2*$^{+/+}$-C21, and $n = 10$ for *Cntnap2*$^{-/-}$-C21). (**G** to **I**) Quantification of grooming time (G), the number of grooming events (H), and digging time (I) with vehicle or C21 ($n = 9$ for *Cntnap2*$^{+/+}$-Veh, $n = 7$ for *Cntnap2*$^{-/-}$-Veh, $n = 8$ for *Cntnap2*$^{+/+}$-C21, and $n = 9$ for *Cntnap2*$^{-/-}$-C21). (**J**) Quantification of interaction time with vehicle or C21 ($n = 8$ for *Cntnap2*$^{+/+}$-Veh, $n = 9$ for *Cntnap2*$^{-/-}$-Veh, $n = 9$ for *Cntnap2*$^{+/+}$-C21, and $n = 11$ for *Cntnap2*$^{-/-}$-C21). The statistical tests involved a paired two-tailed *t* test (B) and two-way ANOVA with Tukey's test (E and F). Data are presented as the mean values ± SEM. *P* values in figure panels: $*P < 0.05$; $**P < 0.01$; $***P < 0.001$.

Downloaded from https://www.science.org at Stanford University on August 25, 2025

the effective designer receptor exclusively activated by designer drugs (DREADD)–mediated activation of RT neurons. Intraperitoneal injection of C21 (2 mg/kg) reduced social preference and increased grooming in *Cntnap2*$^{+/+}$ mice expressing hM3D(Gq) (fig. S8, D and E), recapitulating the behavioral deficits observed in *Cntnap2*$^{-/-}$ mice. Together, these findings demonstrate that RT hyperactivity is both necessary and sufficient to drive ASD-related phenotypes. Suppression of RT activity alleviates behavioral abnormalities in *Cntnap2*$^{-/-}$ mice, highlighting the RT as a potential therapeutic target for ASD intervention.

DISCUSSION

In the present study, we provide comprehensive evidence that RT neurons, a critical inhibitory component of TC circuits, are hyperexcitable in the *Cntnap2*$^{-/-}$ model of ASD. We found (i) an increase in burst firing of RT neurons, (ii) disruption of their synaptic output to TC neurons, and (iii) an elevation of spontaneous in vivo RT population activity. Pharmacological and chemogenetic suppression of RT excitability ameliorates core ASD-related behavioral abnormalities, including hyperlocomotion, impaired social preference, and repetitive behaviors. These findings establish RT hyperexcitability as a key contributor to ASD pathophysiology and highlight its potential as a therapeutic target.

Comorbidities in ASD and *Cntnap2*$^{-/-}$ mice as an animal model

Over the past decades, individuals with ASD and animal models have been characterized by common co-occurring symptoms such as heightened tactile sensitivity (*67*, *68*), attention-deficit/hyperactivity disorder (*33*), sleep disturbances (*11*, *12*, *38*), and epilepsy (*1*, *13*, *42*, *69*). In this study, *Cntnap2*$^{-/-}$ mice show TC hyperexcitability and increased seizure susceptibility alongside core ASD-related deficits, yet we found no evidence of spontaneous seizures of any type, including absence seizures. This suggests that while RT neuron hyperexcitability may prime the TC circuit for abnormal oscillations, spontaneous seizures may require additional cortical or neuromodulatory dysfunction or external triggers. Moreover, compensatory mechanisms within cortical or subcortical circuits may actively suppress pathological rhythms in the absence of acute perturbation. *Cntnap2* encodes a cell adhesion molecule involved in neuronal development, synapse formation, and potassium channel clustering (*1*, *37*, *70*–*72*). In situ hybridization shows that *Cntnap2* mRNA is expressed in RT neurons at levels similar to the cortex and VB (*73*). Loss of Cntnap2 is expected to cause both cell-autonomous and circuit-level changes in RT neurons. At the cellular level, prior studies have shown reduced dendritic spine density (*8*) and abnormal neuronal migration in *Cntnap2*$^{-/-}$ mice (*1*), suggesting that RT neurons may also exhibit disrupted arborization and immature spine development. These structural deficits could impair ion channel localization and synaptic efficacy, contributing to intrinsic and synaptic hyperexcitability in RT neurons. At the circuit level, RT neurons interact closely with the cortex and thalamus, regions with high Cntnap2 expression. Thus, deletion of Cntnap2 in upstream areas, particularly the cortex, may lead to abnormal excitatory input during development, further disrupting RT neuron maturation and compounding the cell-autonomous deficits. Consistent with these mechanisms, *Cntnap2*$^{-/-}$ mice display an increased startle response (*74*), motor abnormalities (*1*), disrupted sleep-wake cycle (*38*), degraded tactile sensation (*4*), and spontaneous seizure-like spike discharges (*38*). Our in vivo EEG and behavioral data support a link between social deficits and both (i) elevated seizure susceptibility and (ii) hyperlocomotor activity, linking epilepsy-related phenotypes to core ASD traits, reinforcing the value of *Cntnap2*$^{-/-}$ mice as a translational model for ASD and its comorbidities.

The RT: A key circuit node in ASD-related behavioral deficits

The thalamus, a central hub for sensory processing, arousal, sleep, and cognition that broadly support social behavior, remains an underexplored yet promising target for elucidating the neural mechanisms underlying ASD pathophysiology. Atypical TC connectivity has been reported in individuals with ASD and is thought to contribute to core symptoms (*17*, *75*). For example, SHANK3 KO mice, a well-established ASD model, exhibit increased TC spike and burst rates alongside ASD-like behavioral phenotypes (*18*). Consistent with these findings, our results revealed enhanced spontaneous and stimulus-evoked oscillatory activity within TC circuits in *Cntnap2*$^{-/-}$ mice, implicating aberrant TC network dynamics as a key contributor to ASD-related dysfunction.

Thalamic oscillations depend critically on the reciprocal connectivity between RT and TC neurons. RT neurons exhibit intrinsic oscillatory activity (*76*, *77*) and provide powerful inhibitory input to TC neurons, generating rhythmic "ping-pong" dynamics whereby RT activation hyperpolarizes TC neurons, which in turn produce RBs that re-excite RT neurons (*78*, *79*). Disruptions in RT activity, whether excessive inhibition or activation, can induce absence seizures characterized by hypersynchronous TC oscillations (*23*, *56*). Increased RT bursting could be linked not only to seizure phenotypes but also to ASD-related behavioral abnormalities, as observed in *Cntnap2*$^{-/-}$ mice, which are also seen in a mouse model of Dravet syndrome (*49*). Notably, recent evidence implicates RT activity in social processing, with elevated RT activity during social interactions and a role in encoding information for recognizing familiar conspecifics (*65*). In line with this, we found that disruption of RT activity correlates with social deficits in *Cntnap2*$^{-/-}$ mice and chemogenetic activation of RT neurons impaired social preference and increased grooming behaviors in *Cntnap2*$^{+/+}$ mice, highlighting the importance of balanced RT activity for proper social behavior and repetitive action control.

Beyond TC loops, RT neurons project to multiple brain regions, including dorsal thalamic nuclei such as the ventrobasal complex (VB) and the lateral habenula, linking RT circuits to diverse functions such as sensory processing, emotional regulation, and pain. For instance, weakened RT-to-TC projections have been associated with chronic sleep disruption–induced hyperalgesia (*64*), and modulation of the somatosensory RT–to–lateral habenula pathway can induce or alleviate depressive-like behaviors (*36*). Our data revealing altered sIPSCs and the PPR in *Cntnap2*$^{-/-}$ mice suggest changes in presynaptic release dynamics and inhibitory input onto TC neurons. In addition to elevated burst firing in RT neurons of *Cntnap2*$^{-/-}$ mice, the known role of Cntnap2 in clustering potassium channels (*70*, *71*) for reliable AP propagation and signal fidelity raises the possibility that its loss may facilitate enhanced AP propagation along RT axons. This could also contribute to increased spontaneous synaptic events and altered presynaptic plasticity at the RT-TC synapses of *Cntnap2*$^{-/-}$ mice. Such changes in presynaptic function could dysregulate broader RT-connected networks involved in sensory, emotional, and cognitive domains and disrupt the excitation/inhibition

Downloaded from https://www.science.org at Stanford University on August 25, 2025

balance during TC processing, potentially driving behavioral deficits observed in *Cntnap2*$^{-/-}$ mice. Future studies should dissect the circuit-specific contribution of RT output to these diverse functions and their influence on social and locomotor behaviors.

PV-expressing RT neurons: A strategic target in ASD-related circuit dysfunction

RT neurons comprise a relatively homogeneous population of GABAergic neurons that robustly express PV (*80*), although subtle variation in molecular and electrophysiological properties and connectivity has been noted (*62*, *63*). These neurons have distinct firing properties and specific projections to TC neurons, playing a critical role in modulating somatosensory processing and seizure activity (*25*). Notably, a reduced number of PV neurons and decreased PV expression have been reported in postmortem brain tissue from individuals with ASD and in animal models of ASD (*5*, *58*, *81*), supporting the "PV hypothesis in ASD" (*82*), which posits that intrinsic and synaptic deficits in PV-expressing neurons contribute causally to ASD pathophysiology. In line with this hypothesis, *Cntnap2*$^{-/-}$ mice, which exhibit core ASD-related behavioral abnormalities, display a reduced number of PV-positive GABAergic interneurons in the hippocampus (*1*) as well as diminished PV-immunoreactive neurons and protein levels in the striatum (*5*), suggesting a role for Cntnap2 in the development of PV-expressing interneurons. Moreover, loss of Cntnap2 function has been shown to impair electrophysiological properties of PV-expressing cortical interneurons that regulate cortical circuits (*83*), induce hyperexcitability in striatal PV interneurons along with hyperactivity (*84*), and increase the maximal firing rate of PV-expressing interneurons in the prefrontal cortex. Collectively, these findings suggest that PV-expressing neurons appear especially susceptible to dysfunction in *Cntnap2*$^{-/-}$ mice, exhibiting both developmental deficits and altered intrinsic electrophysiological characteristics that likely contribute to broader circuit dysfunction–associated ASD. Given that RT neurons constitute a major population of PV-expressing inhibitory neurons in the brain (*55*), they represent a strategically important target for elucidating the cellular and circuit-level mechanisms underlying ASD pathophysiology.

T-type channel–mediated burst firing in RT neurons: A convergent pathway linking Cntnap2 deficiency to ASD

Prior studies have demonstrated reduced burst firing in RT neurons of Ptchd1$^{Y/-}$ mice displaying attention deficits and hyperactivity (*33*) and a state-dependent switch in RT burst patterns during locomotion (*85*). These findings support the hypothesis that enhanced burst firing in RT neurons contributes to ASD-related behavioral phenotypes, as observed in *Cntnap2*$^{-/-}$ mice. Mechanistically, T-type calcium channels regulate burst activity in RT neurons and coordinate synchronized thalamic rhythmicity (*86*). Repetitive bursting also involves R-type calcium channels, small-conductance calcium-activated potassium channels, and calcium-activated nonselective cation channels (*87*–*89*), and so, changes in T-type calcium channel availability alone do not fully predict RB propensity. Nevertheless, disruption in this low-voltage activated calcium influx can lead to aberrant bursting, which is implicated in epilepsy and deficits in sensory and cognitive processing. In a schizophrenia model, Gclm-KO mice exhibit decreased Cav3.3 expression and hypofunction of T-type calcium channels in RT neurons, leading to a hyperpolarizing shift in the threshold for repetitive bursting, thereby altering firing properties (*34*). Furthermore, genome-wide association studies have identified single-nucleotide polymorphisms in the Cav3.3 gene as a risk factor for autism and neuropsychiatric disorders (*90*). Given that Cav3.3 channels are highly enriched in RT (*91*) and that their deletion reduces T-type calcium currents in the RT by ~80%, abolishing RBs (*92*), it is plausible that increased Cav3.3 function contributes to enhanced T-type calcium currents recorded in RT neurons of *Cntnap2*$^{-/-}$ mice, potentially underlying ASD-related behaviors.

Although the precise mechanism by which the loss of Cntnap2 leads to increased T-type calcium currents remains unclear, integrative multiomics analyses have revealed dysregulation of multiple molecular pathways related to neuronal projection, synaptic vesicle transport, and myelin sheath integrity in *Cntnap2*$^{-/-}$ mice (*3*). These findings suggest that elevated T-type calcium channel activity may result from perturbations in intracellular signaling cascades involving heterotrimeric guanine nucleotide–binding protein–coupled receptors (GPCRs) and protein kinases (*93*) and endogenous ligands such as anandamide and endostatin (*94*). Up-regulation or increased availability of T-type calcium channels can enhance low-threshold burst firing without affecting tonic firing rates, allowing neurons to maintain normal tonic activity while exhibiting an increased propensity for burst generation because of altered channel dynamics. Future studies should investigate how Cntnap2 loss influences T-type calcium channel activity, including potential effects on intracellular signaling and channel regulation. Moreover, to better understand the subunit-specific contribution of T-type calcium channel and the interaction between Cntnap2 and these channels in RT neurons, targeted reduction of Cav3 channel expression and Cntnap2 levels in RT neurons via small interfering RNA or short hairpin RNA or CRISPR-based gene editing may help identify specific Cav3 subtypes involved in RT neuron dysfunction and elucidate the mechanism by which Cntnap2 modulates Cav3 channels in the context of ASD.

Pharmacological and neuromodulatory strategies for RT dysfunction in ASD

Z944, a glycinamide compound, is a well-established T-type calcium channel blocker known to inhibit burst firing in RT neurons and reduce absence seizures (*66*). Its therapeutic potential has been extensively explored in various animal models, showing efficacy in alleviating pain (*95*), absence seizures (*66*), and deficits in learning and locomotor function (*96*). While ethosuximide is a well-established first-line treatment for absence seizures, it has broader pharmacological effects and is less selective, which can lead to side effects such as drowsiness. In contrast, Z944 shows higher potency and greater selectivity for neuronal T-type calcium channels (especially in their inactivated state during seizures) and fewer side effects in animal models (*66*, *97*). Notably, systemic administration of Z944 was sufficient to reduce introductory and aggressive behaviors associated with social communication deficits in the GAERS (genetic absence epilepsy rats from Strasbourg) (*98*), and a single injection effectively rescued both social deficits and reduced latency to SWDs in *Cntnap2*$^{-/-}$ mice. These findings suggest that systemic inhibition of T-type calcium channel may be adequate to alleviate ASD-related behavioral impairments, highlighting the therapeutic potential of targeting this pathway. Although we did not check whether Z944 affects intrathalamic oscillations in *Cntnap2*$^{-/-}$ mice, we would expect it to reduce them, as these oscillations are highly dependent on T-type calcium channels (*26*, *53*, *99*).

Downloaded from https://www.science.org at Stanford University on August 25, 2025

Such normalization of TC activity may also contribute to improved ASD-related behaviors in *Cntnap2*$^{-/-}$ mice.

A recent study reported the hyperactivity of the ventral posteromedial nucleus because of HCN2 dysfunction, and early and long-lasting treatment of lamotrigine, a medication used to treat epilepsy and bipolar disorder, resulted in rescue effects that persisted beyond its acute benefits in SHANK3 KO mice (*18*). Although our study did not examine postnatal changes in RT burst activity and their subsequent impact on adult behavioral outcomes, future research should investigate the developmental timing of RT dysfunction onset and whether early administration of Z944 can restore RT function and mitigate long-term behavioral deficits. While the pharmacological approach with Z944 did not directly establish a causal role of T-type calcium channels in RT per se, in ASD behaviors, the results of excitatory and inhibitory DREADD experiments provide complementary support for an RT role, as the PV-Cre and viral strategies specifically targeted RT cells. DREADD-based neuromodulation is emerging as a promising therapeutic strategy. For example, selective enhancement of RT activity has been shown to rescue sleep maintenance and reduce amyloid plaques in both the hippocampus and cortex of an Alzheimer's disease model (*100*), highlighting the therapeutic potential of targeted RT manipulation. Consistent with the effects of Z944, suppression of RT activity using an inhibitory DREADD approach rescued ASD-related pathological behaviors in *Cntnap2*$^{-/-}$ mice. Conversely, excitatory DREADD-mediated activation of RT neurons in *Cntnap2*$^{+/+}$ mice induced deficits in social preference and increased grooming behaviors, demonstrating a causal role of RT neurons in driving ASD-related behaviors. Our rescue experiments suggest that both Z944-mediated pharmacological inhibition and DREADD-based neuromodulation of RT neurons offer a powerful and targeted approach to ameliorate ASD-related behaviors, highlighting a promising strategy for the precision treatment of ASD.

Limitations of the study

While this study focused on RT neurons exhibiting burst firing, we did not assess excitability differences across molecularly distinct RT subpopulations in *Cntnap2*$^{-/-}$ mice, which may differentially modulate TC activity and behavior (*62*, *63*). Future studies using markers such as *Spp1* (encoding secreted phosphoprotein 1) and *Ecel1* (encoding endothelin converting enzyme like 1) may help resolve this heterogeneity. Although we examined composite cortical and thalamic excitatory inputs to RT neurons, the specific contribution of each pathway to the elevated intrathalamic rhythmicity and behavioral phenotypes remains unclear. Moreover, the developmental trajectory of RT hyperexcitability may reflect both direct effects of *Cntnap2* loss and circuit-level compensatory changes. Longitudinal studies will be essential to unravel these mechanisms and fully define the emergence of thalamic dysfunction in this ASD model. In addition, the voltage-clamp experiments documenting altered T-type currents in RT neurons (Fig. 3H) represent a compromise, as it is impractical to completely isolate T currents with somatic recordings of RT cells in brain slices, in which it is nearly impossible to completely control membrane voltage because of their extensive distal dendrites that support burst firing (*101*). Our approach to activate modest currents with near-threshold activation does result in apparent voltage control. Note however that small-conductance calcium-activated potassium channels in RT neurons can be activated by T-type currents in dendrites, resulting in a partial masking of the actual inward Ca^{2+}current (*49*, *77*, *87*, *102*). Even with this caveat, however, we can conclude that the net inward current produced in RT cells under these conditions is larger in *Cntnap2*$^{-/-}$ mice than in *Cntnap2*$^{+/+}$ mice, which would promote burst firing in these cells.

Conclusion and future directions

Overall, this study identifies elevated RT burst firing and aberrant thalamic oscillatory dynamics in *Cntnap2*$^{-/-}$ mice as a key driver of ASD-related behavioral deficits. If this represents a common mechanism underlying ASD circuit pathology across diverse genetic backgrounds, then compounds such as Z944 or subtype-specific T-type calcium channel antagonists targeting Cav3.2 and Cav3.3 channels expressed in RT neurons may offer an effective therapeutic strategy. Future research should aim to elucidate how RT-mediated circuit dynamics throughout the brain influence the broader neurobehavioral landscape of ASD, paving the way for circuit-specific, precision interventions.

MATERIALS AND METHODS

Animals

Experimental *Cntnap2*$^{+/+}$ (WT) and *Cntnap2*$^{-/-}$ (homozygous KO) mice were obtained from heterozygous (HET) crosses of *Cntnap2*$^{+/-}$ (HET) mice and used for EEG recording, behavioral tests, electrophysiology in acute brain slices, and pharmacology experiments. For fiber photometry, optogenetic, and chemogenetic experiments, *Cntnap2*$^{+/+}$ × PV-Cre and *Cntnap2*$^{-/-}$ × PV-Cre mice were generated by crossing male and female *Cntnap2*$^{+/-}$ (HET) × PV-Cre mice, derived from crossing *Cntnap2*$^{-/-}$ × PV-Cre mice (Jax stock no. 008069). For optogenetically induced oscillation experiments, *Cntnap2*$^{+/+}$ × Ai32/Ntsr1-Cre and *Cntnap2*$^{-/-}$ × Ai32/Ntsr1-Cre mice were produced by crossing male and female *Cntnap2*$^{+/-}$ (HET) × Ai32/Ntsr1-Cre mice, which were generated from Ai32 (Jax stock no. 012569) with Ntsr1-cre mice (gift from University of California, Davis). All mice were maintained on a reverse 12-hour dark/light cycle, with experiments conducted during their active (dark) phase. Male mice aged 8 to 14 weeks were used in all experiments except for oscillation recordings, in which equal numbers of males and females were used. Food and water were provided ad libitum. All experimental procedures were approved by the Stanford Administrative Panel on Laboratory Animal Care (protocol no. 12363) and conducted in accordance with National Institutes of Health guidelines.

Virus injection and stereotaxic surgery

Mice were anesthetized with continuous isoflurane (3% for induction and 0.8 to 1.5% for maintenance) and placed in a stereotaxic rig for surgery. A heating pad was used during anesthesia induction and postoperatively, and ophthalmic ointment was applied to protect the eyes throughout the procedure. Stereotaxic coordinates for injections/implantations were as follows: RT (virus injection): anteroposterior, −1.10 mm; mediolateral (ML), ± 2.00 mm; dorsoventral (DV), 3.10 mm. Viral infusions were performed using a 10-min injection (50 nl/min), with a total volume of 350 nl for ex vivo electrophysiology experiments at the RT-TC synapse and chemogenetic modulation. *Cntnap2*$^{+/+}$ × PV-Cre and *Cntnap2*$^{-/-}$ × PV-Cre mice received bilateral injections of AAV2-DIO-hChR2-EYFP, AAV2-hSyn-DIO-hM4D(Gi)-mCherry, or AAV2-hSyn-DIO-hM3D(Gq)-mCherry into the RT, obtained from Addgene (plasmid nos. 26973, 44362, and 44361). After injection, needles were held in place for

Downloaded from https://www.science.org at Stanford University on August 25, 2025

10 min before withdrawal to minimize backflow. Mice were allowed to recover for 3 to 4 weeks before undergoing experiments, including fiber photometry, behavioral assays, electrophysiology, or histological analysis.

Electroencephalogram (EEG)

Cntnap2$^{+/+}$ and *Cntnap2*$^{-/-}$ mice, aged 2 to 4 months, were used for EEG recordings. Mice were anesthetized with isoflurane during the EEG electrode implantation procedure. Under anesthesia, the skull was exposed, and small holes were drilled bilaterally at specific stereotaxic coordinates (anteroposterior, −1.0 mm; ML, ±2.0 mm) for the somatosensory cortex to accommodate electrode placement. Sterilized gold pins were secured to the skull at the designated recording sites using adhesive, with a reference electrode positioned in the cerebellum. Following electrode placement, the mice were allowed to recover in their home cages for at least 3 days to ensure stable electrode integration. EEG recordings were conducted in a quiet, controlled environment during the (dark) active phase. Mice were connected to an Open Ephys/Intan headstage recording system via lightweight, flexible cables for data acquisition. EEG signals were amplified and filtered at 2 kHz, with continuous recordings performed for 10 min following intraperitoneal injection of PTZ (Sigma-Aldrich; 20 mg/kg). EEG data were analyzed offline using custom MATLAB scripts to manually process the recorded signals.

Behavioral tests

Behavioral tests were conducted using male mice, aged 8 to 12 weeks, because *Cntnap2*$^{-/-}$ female mice show no significant behavioral deficits (*41*). Tests were performed during light-off periods. Subject mice were given at least 2 days of rest between different tests to minimize stress or carryover effects. Behavioral data were recorded using a video camera positioned above the testing area. Analysis was performed manually or using custom MATLAB scripts designed for the specific behavioral paradigms.

Open-field test

A subject mouse was placed into the center of the open-field box (white acrylic chamber, 50 by 50 by 50 cm) and recorded for 10 min for comparisons of *Cntnap2*$^{+/+}$ and *Cntnap2*$^{-/-}$ mice or 30 min for Z944 and DREADD experiments. The chamber was illuminated at ~100 lux. Mouse movements were tracked and analyzed using customized Python scripts.

Three-chamber test

Subject mice were isolated for 24 hours before testing. The three-chambered apparatus (white acrylic chamber, 40 by 20 by 25 cm) consisted of left, center, and right chambers arranged in a row, with two entrances connecting the center chamber to the side chambers. The test consisted of two 10-min phases. In the first phase, the subject mouse was introduced into the center chamber and allowed to freely explore all three chambers with empty wire cages positioned in the left and right chambers. In the second phase, one wire cage was replaced with a novel object (O), while another cage contained a stranger mouse (S), which was a C57BL/6J strain and sex and age matched to the subject mouse. During the interval between phases, the subject mouse was gently guided to the center chamber, the entrances to the side chambers were temporarily blocked by barriers, and then the barriers were removed to let the subject mouse move freely in the arena. The center chamber was illuminated at ~100 lux. The time spent in the chambers containing the stranger mouse or object was recorded and analyzed using custom Python scripts. The sociality index was calculated as $[T_{mouse} - T_{object}]/[T_{mouse} + T_{object}]$, where T_{mouse} and T_{object} represent the time spent interacting with the stranger mouse and object, respectively. To further obtain detailed information about social interaction, the time spent in direct physical contact with wire cages on both sides was manually scored in a blind manner. Between each measurement, the apparatus was cleaned with 75% ethanol to minimize residual olfactory cues.

Grooming behavior

A subject mouse was placed in a new home cage containing fresh bedding and allowed to freely explore for 20 min. The center of the cage was illuminated at ~100 lux. The time spent digging and self-grooming during the final 10 min was recorded manually in a blinded manner. Digging was defined as the mouse using its head or forelimbs to displace bedding. Self-grooming was defined as the mouse stroking or scratching its face or body or licking its body.

Reciprocal interactions

A subject mouse, aged 8 to 12 weeks, was placed in a chamber (40 by 20 by 25 cm) and allowed to habituate for 10 min. Following habituation, a novel conspecific mouse, matched for genotype, age, sex, and/or treatment, was introduced into a neutral area of the chamber. The time spent in social interactions, including nose-to-anogenital sniffing and nose-to-nose sniffing, was recorded manually by an observer blinded to the experimental conditions of the test mouse.

Thalamic slice preparation

Mice were anesthetized with isoflurane and transcardially perfused with ice-cold sucrose-based cutting solution containing 234 mM sucrose, 11 mM glucose, 26 mM $NaHCO_3$, 2.5 mM KCl, 1.25 mM NaH_2PO_4, 10 mM $MgSO_4$, and 0.5 mM $CaCl_2$ (310 mosmol). Horizontal slices (270 μm) containing RT and TC regions were sectioned using a vibratome (VT1200, Leica) with a slicing speed of 0.07 to 0.08 mm/s. Slices were incubated on a Brain Slice Keeper 4 (Auto-Mate Scientific, Berkeley, CA); continuously oxygenated in warm (~32°C) artificial cerebrospinal fluid (ACSF) containing 10 mM glucose, 26 mM $NaHCO_3$, 2.5 mM KCl, 1.25 mM $NaHPO_4$, 2 mM $MgSO_4$, 2 mM $CaCl_2$, and 126 mM NaCl (290 to 300 mosmol) for 1 hour; and then transferred to room temperature (~21° to 23°C) for at least 1 hour before electrophysiological recording.

Extracellular thalamic oscillations

For oscillation recordings, 400-μm-thick brain slices from *Cntnap2*$^{+/+}$ and *Cntnap2*$^{-/-}$ juvenile mice (P21 to P25) were placed in a humidified, oxygenated interface recording chamber and perfused with oxygenated ACSF with low magnesium (0.5 mM) at a flow rate of 2 ml/min, maintained at 32° to 34°C. To ensure stable perfusion, squares of lens paper were placed beneath and on top of the slice, with a small cutout in the top layer to allow electrode access, and the preparation was secured using platinum bars. To mitigate gradual GABA depletion, L-glutamine (300 μM), a metabolic substrate for GABA synthesis, was added to the ACSF as described by Bryant *et al.* (*103*). For spontaneous oscillation recordings, a tungsten electrode (50 to 100 kilohms; FHC) was placed in the VB, and recordings were conducted continuously for 10 min. Optogenetically evoked oscillations were induced by delivering 490-nm blue laser pulses (1-ms duration) to the RT and VB regions every 30 s for 10 min. For electrical

Downloaded from https://www.science.org at Stanford University on August 25, 2025

stimulation–induced oscillations, square current pulses were delivered through two parallel tungsten electrodes (50 to 100 kilohms; FHC) placed 50 to 100 μm apart in the i.c. to stimulate both cortical and thalamic axons. Electrical stimuli were 100 μs in duration and 50 V in amplitude and were delivered every 30 s for 10 min. Extracellular potentials were recorded using a tungsten electrode (50 to 100 kilohms; FHC) placed in the VB. One experiment was performed per slice, and only slices with a spontaneous bursting frequency of at least five bursts per minute were included in the analyses. Oscillation spike detection and parameter analyses were performed as described by Sohal and Huguenard (*104*). Briefly, spikes were identified as slope deflections greater than three times the threshold, where the threshold was defined as the root mean square of background noise during baseline sweeps. Bursts were defined as clusters of spikes (greater than or equal to two spikes with <6-ms maximum interval in burst). Oscillations were defined as clusters of bursts (greater than or equal to two bursts with <0.1-s maximum interval in oscillation). Spontaneous oscillations were defined as greater than or equal to one event per 30-s trial over 10 min. The detection criteria for bursting and oscillatory activity were refined through manual validation using at least three randomly selected datasets. The threshold and detection criteria were applied uniformly across all recordings. Data and statistical analyses were conducted using MATLAB 2023b (MathWorks) and GraphPad Prism 9.

Patch-clamp electrophysiology

Whole-cell patch-clamp recordings of RT neurons were conducted using glass patch pipettes (3 to 5 megohms) filled with an intracellular solution containing 126 mM K-gluconate, 4 mM KCl, 2 mM Mg-ATP, 0.3 mM GTP-tris, and 10 mM phosphocreatine, with pH adjusted to 7.4 using KOH (290 mosmol). For current-clamp recordings, cells were held at a resting membrane potential of ~−70 mV, with steady intracellular current applied throughout the recording. Experiments were performed in the presence of kynurenic acid and gabazine (SR-95531) to block fast excitatory and inhibitory synaptic transmissions, respectively. Pipette capacitance was compensated, and the bridge balance was adjusted. Evoked APs were elicited by injecting 1-s-duration current steps of increasing amplitude (0 to 300 pA). Rheobase for burst firing was measured by applying a gradually increasing current step (5-pA increments, 100 ms each), and the threshold was defined as the minimal current amplitude that reliably evoked burst firing. The exported traces of APs were further analyzed, and the first and second derivatives (dV/dt and d^2V/dt^2, respectively) were calculated using pClampFit 10.7 and custom MATLAB (MathWorks) code. For voltage-clamp recordings of inhibitory synaptic events, including sIPSCs and oIPSCs (optogenetically evoked IPSCs), the pipette solution contained 135 mM CsCl, 10 mM Hepes, 10 mM EGTA, 2 mM $MgCl_2$, and 5 mM QX-314, with pH adjusted to 7.4 using CsOH (290 mosmol). The membrane potential was held at −70 mV, and signals were recorded using a Multiclamp 700A amplifier with pClamp 10.7 software (Axon Instruments, San Jose, CA) at a sampling rate of 50 kHz, with low-pass filtering at 10 kHz. sIPSCs and oIPSCs were detected using custom software (Wdetecta, JRH). To ensure voltage control and isolate low-threshold T-type calcium currents, we applied a steady-state inactivation protocol (*26*, *102*), confirmed in our lab, in which peak latencies remained constant following steps to −55 mV from a range of hyperpolarizing conditioning potentials (−105 to −65 mV) under a holding potential of −60 mV. For analysis, we selected RT neurons that exhibited consistent peak latencies, and peak amplitudes in the interval between the arrows in the indicated protocol were normalized to cell capacitance to yield current density. Data from unstable recordings were excluded if (i) the series resistance increased by more than 20% from the initial value or (ii) the holding current changed by more than 100 pA.

Optogenetic stimulation

Mice that underwent stereotaxic injection of AAV5.EF1a.DIO.hChR2(H134R)-EYFP.WPRE.hGH virus into the RT region (anteroposterior, −1.1 to −1.2 mm; ML, ±2.0 mm; DV, −3.0 mm) of *Cntnap2*$^{+/+}$ × PV-Cre and *Cntnap2*$^{-/-}$ × PV-Cre mice were euthanized, and fresh brain slices were prepared for patch-clamp physiology as described above. RT neurons expressing hChR2-EYFP were activated with 475-nm light at an intensity of 1.9 mW/cm^2. We applied 1-ms pulses of blue light-emitting diode light at frequencies of 5, 10, 20, 30, and 50 Hz for 5 s to stimulate presynaptic release, as previously described.

In vivo fiber photometry

Fiber photometry was used to record fluorescence signals in vivo. For fiber photometry recordings of calcium activity, AAV2/9-EF1a-DIO-GCaMP6f was injected at the following coordinates—anteroposterior, −1.10 mm; ML, ±2.00 mm; DV, 3.15 mm—into *Cntnap2*$^{+/+}$ × PV-cre and *Cntnap2*$^{-/-}$ × PV-cre mice. Optic fiber cannulae with a 200-μm core, 0.39 numerical aperture, and 1.25-mm-diameter ferrule (RWD Life Science) were implanted at the following coordinates—anteroposterior, −1.10 mm; ML, ±2.00 mm; DV, 3.00 mm—from bregma for the RT. The 4.0-mm-long optic fiber cannulae were used for the RT and fixed to the skull with dental cement (C&B Metabond, Parkell). Animals were allowed to recover from surgery for 3 weeks before the recording experiments. In vivo fiber photometry recordings were performed using a dual-color multichannel fiber photometry system (R811, RWD Life Science) with a low-autofluorescence 1-to-4 fan-out bundled fiber patch cord with a 200-μm core, 0.39 numerical aperture, and 1.25-mm-diameter ferrule. To account for potential bleaching and quenching effects related to vigilance states, we used an isosbestic correction method. Specifically, we simultaneously recorded fluorescence signals at 470-nm (calcium-dependent) and 410-nm (isosbestic, calcium-independent) wavelengths. We then calculated $\Delta F/F$ by normalizing the 470-nm signal to the 410-nm signal. This ratiometric approach effectively minimizes confounding effects from photobleaching and state-dependent signal fluctuations, consistent with established methodologies (*105*). All experiments were conducted during the animals' light cycle (Zeitgeber times 1 to 12). Illumination was controlled using an external light source positioned above the arena. Throughout the sessions, animals remained awake, as confirmed by video monitoring and the absence of sleep-like postures or prolonged immobility. To minimize stress and environmental novelty, mice were habituated for at least 1 hour in the experimental room, followed by an additional 10 min in the arena or cages before recording. For the light-dark experiment, animals were first recorded for 10 min under the light condition, after which the light was turned off and recording continued for an additional 10 min without disconnecting the fiber. For the social interaction experiment, mice were initially recorded alone for 10 min, followed by the introduction of a novel social partner into the arena, and recording resumed for another 10 min. For the novel object experiment, animals were first placed in a clean cage, recorded for 10 min, and then transferred to a cage containing novel

Downloaded from https://www.science.org at Stanford University on August 25, 2025

objects for an additional 10-min session. For the PTZ experiment, mice were recorded in the arena for 10 min before intraperitoneal injection of PTZ (20 mg/kg), after which recording continued for another 10 min.

The data from fiber photometry were processed and analyzed as follows: The photometry signal value F was calculated as F_{470}/F_{410}. $\Delta F/F$ was then derived using the formula $\Delta F/F = (F - F_0)/F_0$, where F_0 is the median of the photometry signal. Only calcium signals greater than 3 SD were treated as events, detected using the findpeaks function in MATLAB.

Quantification and statistical analysis

All bar graphs indicate the means, and all error bars represent ±SEM. Statistical analyses were performed using GraphPad Prism 9 (GraphPad Software, La Jolla, CA), Excel (Microsoft), and custom MATLAB programs (MathWorks, Natick, MA). Normally distributed data with equal variance were analyzed using a t test (two-tailed, unpaired or paired), one-way analysis of variance (ANOVA), or two-way ANOVA, followed by Tukey's multiple comparison test. A mixed-effects model [restricted maximum likelihood (REML)] was used in GraphPad Prism, with genotype as a fixed effect and mouse ID as a random effect, to account for repeated measurements from the same animal. This statistical approach was applied in Figs. 2 (C, E, and H), 3 (C, D, F, and H), 4 (A and D), and 5D to appropriately control for intermouse variability. Statistical values are denoted as follows: $^*P < 0.05$, $^{**}P < 0.01$, and $^{***}P < 0.001$.

Supplementary Materials

The PDF file includes:
Figs. S1 to S8
Legends for movies S1 to S8

Other Supplementary Material for this manuscript includes the following:
Movies S1 to S8

REFERENCES AND NOTES

1. O. Peñagarikano, B. S. Abrahams, E. I. Herman, K. D. Winden, A. Gdalyahu, H. Dong, L. I. Sonnenblick, R. Gruver, J. Almajano, A. Bragin, P. Golshani, J. T. Trachtenberg, E. Peles, D. H. Geschwind, Absence of CNTNAP2 leads to epilepsy, neuronal migration abnormalities, and core autism-related deficits. *Cell* **147**, 235–246 (2011).
2. K. R. Cording, E. M. Tu, H. Wang, A. H. Agopyan-Miu, H. S. Bateup, Cntnap2 loss drives striatal neuron hyperexcitability and behavioral inflexibility. *eLife* **13**, RP100162 (2024).
3. W. E. Jang, J. H. Park, G. Park, G. Bang, C. H. Na, J. Y. Kim, K.-Y. Kim, K. P. Kim, C. Y. Shin, J.-Y. An, Y.-S. Lee, M.-S. Kim, Cntnap2-dependent molecular networks in autism spectrum disorder revealed through an integrative multi-omics analysis. *Mol. Psychiatry* **28**, 810–821 (2023).
4. H. C. Wang, D. E. Feldman, Degraded tactile coding in the Cntnap2 mouse model of autism. *Cell Rep.* **43**, 114612 (2024).
5. E. Lauber, F. Filice, B. Schwaller, Dysregulation of parvalbumin expression in the *Cntnap2*$^{-/-}$ mouse model of autism spectrum disorder. *Front. Mol. Neurosci.* **11**, 262 (2018).
6. M. J. Gandal, J. R. Haney, B. Wamsley, C. X. Yap, S. Parhami, P. S. Emani, N. Chang, G. T. Chen, G. D. Hoftman, D. De Alba, G. Ramaswami, C. L. Hartl, A. Bhattacharya, C. Luo, T. Jin, D. Wang, R. Kawaguchi, D. Quintero, J. Ou, Y. E. Wu, N. N. Parikshak, V. Swarup, T. G. Belgard, M. Gerstein, B. Pasaniuc, D. H. Geschwind, Broad transcriptomic dysregulation occurs across the cerebral cortex in ASD. *Nature* **611**, 532–539 (2022).
7. H. Won, H.-R. Lee, H. Y. Gee, W. Mah, J.-I. Kim, J. Lee, S. Ha, C. Chung, E. S. Jung, Y. S. Cho, S.-G. Park, J.-S. Lee, K. Lee, D. Kim, Y. C. Bae, B.-K. Kaang, M. G. Lee, E. Kim, Autistic-like social behaviour in Shank2-mutant mice improved by restoring NMDA receptor function. *Nature* **486**, 261–265 (2012).
8. M. T. Lazaro, J. Taxidis, T. Shuman, I. Bachmutsky, T. Ikrar, R. Santos, G. M. Marcello, A. Mylavarapu, S. Chandra, A. Foreman, R. Goli, D. Tran, N. Sharma, M. Azhdam, H. Dong, K. Y. Choe, O. Peñagarikano, S. C. Masmanidis, B. Rácz, X. Xu, D. H. Geschwind, P. Golshani, Reduced prefrontal synaptic connectivity and disturbed oscillatory population dynamics in the CNTNAP2 model of autism. *Cell Rep.* **27**, 2567–2578.e6 (2019).
9. J. K. Kern, M. H. Trivedi, C. R. Garver, B. D. Grannemann, A. A. Andrews, J. S. Savla, D. G. Johnson, J. A. Mehta, J. L. Schroeder, The pattern of sensory processing abnormalities in autism. *Autism* **10**, 480–494 (2006).
10. E. J. Marco, L. B. N. Hinkley, S. S. Hill, S. S. Nagarajan, Sensory processing in autism: A review of neurophysiologic findings. *Pediatr. Res.* **69**, 48R–54R (2011).
11. M. O. Mazurek, K. Sohl, Sleep and behavioral problems in children with autism spectrum disorder. *J. Autism Dev. Disord.* **46**, 1906–1915 (2016).
12. M. C. Souders, T. B. A. Mason, O. Valladares, M. Bucan, S. E. Levy, D. S. Mandell, T. E. Weaver, J. Pinto-Martin, Sleep behaviors and sleep quality in children with autism spectrum disorders. *Sleep* **32**, 1566–1578 (2009).
13. S. Lukmanji, S. A. Manji, S. Kadhim, K. M. Sauro, E. C. Wirrell, C.-S. Kwon, N. Jetté, The co-occurrence of epilepsy and autism: A systematic review. *Epilepsy Behav.* **98**, 238–248 (2019).
14. J. B. Ewen, A. R. Marvin, K. Law, P. H. Lipkin, Epilepsy and autism severity: A study of 6,975 children. *Autism Res.* **12**, 1251–1259 (2019).
15. A. Nair, J. M. Treiber, D. K. Shukla, P. Shih, R.-A. Müller, Impaired thalamocortical connectivity in autism spectrum disorder: A study of functional and anatomical connectivity. *Brain* **136**, 1942–1955 (2013).
16. M. Schuetze, M. T. M. Park, I. Y. Cho, F. P. MacMaster, M. M. Chakravarty, S. L. Bray, Morphological alterations in the thalamus, striatum, and pallidum in autism spectrum disorder. *Neuropsychopharmacology* **41**, 2627–2637 (2016).
17. T. Iidaka, T. Kogata, Y. Mano, H. Komeda, Thalamocortical hyperconnectivity and amygdala-cortical hypoconnectivity in male patients with autism spectrum disorder. *Front. Psych.* **10**, 252 (2019).
18. B. Guo, T. Liu, S. Choi, H. Mao, W. Wang, K. Xi, C. Jones, N. D. Hartley, D. Feng, Q. Chen, Y. Liu, R. D. Wimmer, Y. Xie, N. Zhao, J. Ou, M. A. Arias-Garcia, D. Malhotra, Y. Liu, S. Lee, S. Pasqualoni, R. J. Kast, M. Fleishman, M. M. Halassa, S. Wu, Z. Fu, Restoring thalamocortical circuit dysfunction by correcting HCN channelopathy in Shank3 mutant mice. *Cell Rep. Med.* **5**, 101534 (2024).
19. S. Ahrens, S. Jaramillo, K. Yu, S. Ghosh, G.-R. Hwang, R. Paik, C. Lai, M. He, Z. J. Huang, B. Li, ErbB4 regulation of a thalamic reticular nucleus circuit for sensory selection. *Nat. Neurosci.* **18**, 104–111 (2015).
20. G. Vantomme, Z. Rovó, R. Cardis, E. Béard, G. Katsioudi, A. Guadagno, V. Perrenoud, L. M. J. Fernandez, A. Lüthi, A thalamic reticular circuit for head direction cell tuning and spatial navigation. *Cell Rep.* **31**, 107747 (2020).
21. J.-H. Lee, C.-F. V. Latchoumane, J. Park, J. Kim, J. Jeong, K.-H. Lee, H.-S. Shin, The rostroventral part of the thalamic reticular nucleus modulates fear extinction. *Nat. Commun.* **10**, 4637 (2019).
22. L. D. Lewis, J. Voigts, F. J. Flores, L. I. Schmitt, M. A. Wilson, M. M. Halassa, E. N. Brown, Thalamic reticular nucleus induces fast and local modulation of arousal state. *eLife* **4**, e08760 (2015).
23. X. Zhang, X. Yu, M. Tuo, Z. Zhao, J. Wang, T. Jiang, M. Zhang, Y. Wang, Y. Sun, Parvalbumin neurons in the anterior nucleus of thalamus control absence seizures. *Epilepsia Open* **8**, 1002–1012 (2023).
24. P.-F. Liu, Y. Wang, L. Xu, A.-F. Xiang, M.-Z. Liu, Y.-B. Zhu, X. Jia, R. Zhang, J.-B. Li, L. Zhang, D. Mu, Modulation of itch and pain signals processing in ventrobasal thalamus by thalamic reticular nucleus. *iScience* **25**, 103625 (2022).
25. A. Clemente-Perez, S. R. Makinson, B. Higashikubo, S. Brovarney, F. S. Cho, A. Urry, S. S. Holden, M. Wimer, C. Dávid, L. E. Fenno, L. Acsády, K. Deisseroth, J. T. Paz, Distinct thalamic reticular cell types differentially modulate normal and pathological cortical rhythms. *Cell Rep.* **19**, 2130–2142 (2017).
26. J. Huguenard, D. Prince, A novel T-type current underlies prolonged Ca^{2+}-dependent burst firing in GABAergic neurons of rat thalamic reticular nucleus. *J. Neurosci.* **12**, 3804–3817 (1992).
27. C. L. Cox, J. R. Huguenard, D. A. Prince, Nucleus reticularis neurons mediate diverse inhibitory effects in thalamus. *Proc. Natl. Acad. Sci. U.S.A.* **94**, 8854–8859 (1997).
28. C. L. Cox, J. R. Huguenard, D. A. Prince, Heterogeneous axonal arborizations of rat thalamic reticular neurons in the ventrobasal nucleus. *J. Comp. Neurol.* **366**, 416–430 (1996).
29. V. S. Sohal, M. M. Huntsman, J. R. Huguenard, Reciprocal inhibitory connections regulate the spatiotemporal properties of intrathalamic oscillations. *J. Neurosci.* **20**, 1735–1745 (2000).
30. M. M. Halassa, J. H. Siegle, J. T. Ritt, J. T. Ting, G. Feng, C. I. Moore, Selective optical drive of thalamic reticular nucleus generates thalamic bursts and cortical spindles. *Nat. Neurosci.* **14**, 1118–1120 (2011).
31. C. M. Schofield, M. Kleiman-Weiner, U. Rudolph, J. R. Huguenard, A gain in $GABA_A$ receptor synaptic strength in thalamus reduces oscillatory activity and absence seizures. *Proc. Natl. Acad. Sci. U.S.A.* **106**, 7630–7635 (2009).
32. P. M. Fogerson, J. R. Huguenard, Tapping the brakes: Cellular and synaptic mechanisms that regulate thalamic oscillations. *Neuron* **92**, 687–704 (2016).

Downloaded from https://www.science.org at Stanford University on August 25, 2025

33. M. F. Wells, R. D. Wimmer, L. I. Schmitt, G. Feng, M. M. Halassa, Thalamic reticular impairment underlies attention deficit in Ptchd1(Y/-) mice. *Nature* **532**, 58–63 (2016).
34. C. El Khoueiry, J.-H. Cabungcal, Z. Rovó, M. Fournier, K. Q. Do, P. Steullet, Developmental oxidative stress leads to T-type Ca^{2+} channel hypofunction in thalamic reticular nucleus of mouse models pertinent to schizophrenia. *Mol. Psychiatry* **27**, 2042–2051 (2022).
35. X. Zhu, J.-H. Cabungcal, M. Cuenod, D. L. Uliana, K. Q. Do, A. A. Grace, Thalamic reticular nucleus impairments and abnormal prefrontal control of dopamine system in a developmental model of schizophrenia: prevention by N-acetylcysteine. *Mol. Psychiatry* **26**, 7679–7689 (2021).
36. X.-Y. Wang, X. Xu, R. Chen, W.-B. Jia, P.-F. Xu, X.-Q. Liu, Y. Zhang, X.-F. Liu, Y. Zhang, The thalamic reticular nucleus-lateral habenula circuit regulates depressive-like behaviors in chronic stress and chronic pain. *Cell Rep.* **42**, 113170 (2023).
37. R. Paterno, J. R. Marafiga, H. Ramsay, T. Li, K. A. Salvati, S. C. Baraban, Hippocampal gamma and sharp-wave ripple oscillations are altered in a Cntnap2 mouse model of autism spectrum disorder. *Cell Rep.* **37**, 109970 (2021).
38. A. M. Thomas, M. D. Schwartz, M. D. Saxe, T. S. Kilduff, Cntnap2 knockout rats and mice exhibit epileptiform activity and abnormal sleep–wake physiology. *Sleep* **40**, zsw026 (2017).
39. A. N. Mohapatra, R. Jabarin, N. Ray, S. Netser, S. Wagner, Impaired emotion recognition in Cntnap2-deficient mice is associated with hyper-synchronous prefrontal cortex neuronal activity. *Mol. Psychiatry* **30**, 1440–1452 (2024).
40. S. Jurgensen, P. E. Castillo, Selective dysregulation of hippocampal inhibition in the mouse lacking autism candidate gene *CNTNAP2*. *J. Neurosci.* **35**, 14681–14687 (2015).
41. M. S. Dawson, K. Gordon-Fleet, L. Yan, V. Tardos, H. He, K. Mui, S. Nawani, Z. Asgarian, M. Catani, C. Fernandes, U. Drescher, Sexual dimorphism in the social behaviour of Cntnap2-null mice correlates with disrupted synaptic connectivity and increased microglial activity in the anterior cingulate cortex. *Commun. Biol.* **6**, 846 (2023).
42. S. S. Jeste, R. Tuchman, Autism spectrum disorder and epilepsy: Two sides of the same coin? *J. Child Neurol.* **30**, 1963–1971 (2015).
43. S. N. Mandhane, K. Aavula, T. Rajamannar, Timed pentylenetetrazol infusion test: A comparative analysis with s.c.PTZ and MES models of anticonvulsant screening in mice. *Seizure* **16**, 636–644 (2007).
44. E. L. Hill-Yardin, A. Argyropoulos, S. Hosie, G. Rind, P. Anderson, A. J. Hannan, T. J. O'Brien, Reduced susceptibility to induced seizures in the Neuroligin-3^{R451C} mouse model of autism. *Neurosci. Lett.* **589**, 57–61 (2015).
45. G. M. Jacobson, L. J. Voss, S. M. Melin, J. P. Mason, R. T. Cursons, D. A. Steyn-Ross, M. L. Steyn-Ross, J. W. Sleigh, Connexin36 knockout mice display increased sensitivity to pentylenetetrazol-induced seizure-like behaviors. *Brain Res.* **1360**, 198–204 (2010).
46. A. Ruszczak, P. Poznański, A. Leśniak, M. Łazarczyk, D. Skiba, A. Nawrocka, K. Gaweł, J. Paszkiewicz, M.-E. Mickael, M. Sacharczuk, Susceptibility to pentylenetetrazole-induced seizures in mice with distinct activity of the endogenous opioid system. *Int. J. Mol. Sci.* **25**, 6978 (2024).
47. J. V. Erum, D. V. Dam, P. P. D. Deyn, PTZ-induced seizures in mice require a revised Racine scale. *Epilepsy Behav.* **95**, 51–55 (2019).
48. W. Löscher, M. Fiedler, The role of technical, biological and pharmacological factors in the laboratory evaluation of anticonvulsant drugs. VI. Seasonal influences on maximal electroshock and pentylenetetrazol seizure thresholds. *Epilepsy Res.* **25**, 3–10 (1996).
49. S. Ritter-Makinson, A. Clemente-Perez, B. Higashikubo, F. S. Cho, S. S. Holden, E. Bennett, A. Chkhaidze, O. H. J. Eelkman Rooda, M.-C. Cornet, F. E. Hoebeek, K. Yamakawa, M. R. Cilio, B. Delord, J. T. Paz, Augmented reticular thalamic bursting and seizures in Scn1a-Dravet syndrome. *Cell Rep.* **26**, 54–64.e6 (2019).
50. C. D. Makinson, B. S. Tanaka, J. M. Sorokin, J. C. Wong, C. A. Christian, A. L. Goldin, A. Escayg, J. R. Huguenard, Regulation of thalamic and cortical network synchrony by Scn8a. *Neuron* **93**, 1165–1179.e6 (2017).
51. J. T. Paz, A. S. Bryant, K. Peng, L. Fenno, O. Yizhar, W. N. Frankel, K. Deisseroth, J. R. Huguenard, A new mode of corticothalamic transmission revealed in the Gria4−/− model of absence epilepsy. *Nat. Neurosci.* **14**, 1167–1173 (2011).
52. C. L. Kyuyoung, J. R. Huguenard, Modulation of short-term plasticity in the corticothalamic circuit by group III metabotropic glutamate receptors. *J. Neurosci.* **34**, 675–687 (2014).
53. A. C. Lu, C. K. Lee, M. Kleiman-Weiner, B. Truong, M. Wang, J. R. Huguenard, M. P. Beenhakker, Nonlinearities between inhibition and T-type calcium channel activity bidirectionally regulate thalamic oscillations. *eLife* **9**, e59548 (2020).
54. R. B. Jacobsen, D. Ulrich, J. R. Huguenard, GABA(B) and NMDA receptors contribute to spindle-like oscillations in rat thalamus in vitro. *J. Neurophysiol.* **86**, 1365–1375 (2001).
55. G. Hou, A. G. Smith, Z.-W. Zhang, Lack of intrinsic GABAergic connections in the thalamic reticular nucleus of the mouse. *J. Neurosci.* **36**, 7246–7252 (2016).
56. M. Abdelaal, M. Midorikawa, T. Suzuki, K. Kobayashi, N. Takata, M. Miyata, M. Mimura, K. Tanaka, Dysfunction of parvalbumin-expressing cells in the thalamic reticular nucleus induces cortical spike-and-wave discharges and an unconscious state. *Brain Commun.* **4**, fcac010 (2022).
57. M. Wöhr, D. Orduz, P. Gregory, H. Moreno, U. Khan, K. J. Vörckel, D. P. Wolfer, H. Welzl, D. Gall, S. N. Schiffmann, B. Schwaller, Lack of parvalbumin in mice leads to behavioral deficits relevant to all human autism core symptoms and related neural morphofunctional abnormalities. *Transl. Psychiatry* **5**, e525 (2015).
58. F. Filice, K. J. Vörckel, A. Ö. Sungur, M. Wöhr, B. Schwaller, Reduction in parvalbumin expression not loss of the parvalbumin-expressing GABA interneuron subpopulation in genetic parvalbumin and shank mouse models of autism. *Mol. Brain* **9**, 10 (2016).
59. G. Calfa, W. Li, J. M. Rutherford, L. Pozzo-Miller, Excitation/inhibition imbalance and impaired synaptic inhibition in hippocampal area CA3 of *Mecp2* knockout mice: E/I imbalance in Mecp2 knockout hippocampus. *Hippocampus* **25**, 159–168 (2015).
60. A. Caballero, E. Flores-Barrera, D. R. Thomases, K. Y. Tseng, Downregulation of parvalbumin expression in the prefrontal cortex during adolescence causes enduring prefrontal disinhibition in adulthood. *Neuropsychopharmacology* **45**, 1527–1535 (2020).
61. S.-S. Jang, N. Agranonik, J. R. Huguenard, Actions of the anti-seizure drug carbamazepine in the thalamic reticular nucleus: Potential mechanism of aggravating absence seizures. bioRxiv 636080 [Preprint] (2025). https://doi.org/10.1101/2025.02.03.636080.
62. Y. Li, V. G. Lopez-Huerta, X. Adiconis, K. Levandowski, S. Choi, S. K. Simmons, M. A. Arias-Garcia, B. Guo, A. Y. Yao, T. R. Blosser, R. D. Wimmer, T. Aida, A. Atamian, T. Naik, X. Sun, D. Bi, D. Malhotra, C. C. Hession, R. Shema, M. Gomes, T. Li, E. Hwang, A. Krol, M. Kowalczyk, J. Peça, G. Pan, M. M. Halassa, J. Z. Levin, Z. Fu, G. Feng, Distinct subnetworks of the thalamic reticular nucleus. *Nature* **583**, 819–824 (2020).
63. N. D. Hartley, A. Krol, S. Choi, N. Rome, K. Levandowski, S. Pasqualoni, C. Jones, J. Tian, S. Lee, H. Lee, R. Kast, G. Feng, Z. Fu, Distinct structural and functional connectivity of genetically segregated thalamoreticular subnetworks. *Cell Rep.* **43**, 115037 (2024).
64. W. Ding, L. Yang, E. Shi, B. Kim, S. Low, K. Hu, L. Gao, P. Chen, W. Ding, D. Borsook, A. Luo, J. H. Choi, C. Wang, O. Akeju, J. Yang, C. Ran, K. L. Schreiber, J. Mao, Q. Chen, G. Feng, S. Shen, The endocannabinoid N-arachidonoyl dopamine is critical for hyperalgesia induced by chronic sleep disruption. *Nat. Commun.* **14**, 6696 (2023).
65. F. Wang, H. Sun, M. Chen, B. Feng, Y. Lu, M. Lyu, D. Cui, Y. Zhai, Y. Zhang, Y. Zhu, C. Wang, H. Wu, X. Ma, F. Zhu, Q. Wang, Y. Li, The thalamic reticular nucleus orchestrates social memory. *Neuron* **112**, 2368–2385.e11 (2024).
66. E. Tringham, K. L. Powell, S. M. Cain, K. Kuplast, J. Mezeyova, M. Weerapura, C. Eduljee, X. Jiang, P. Smith, J.-L. Morrison, N. C. Jones, E. Braine, G. Rind, M. Fee-Maki, D. Parker, H. Pajouhesh, M. Parmar, T. J. O'Brien, T. P. Snutch, T-type calcium channel blockers that attenuate thalamic burst firing and suppress absence seizures. *Sci. Transl. Med.* **4**, 121ra19 (2012).
67. C. Cascio, F. McGlone, S. Folger, V. Tannan, G. Baranek, K. A. Pelphrey, G. Essick, Tactile perception in adults with autism: A multidimensional psychophysical study. *J. Autism Dev. Disord.* **38**, 127–137 (2008).
68. L. L. Orefice, A. L. Zimmerman, A. M. Chirila, S. J. Sleboda, J. P. Head, D. D. Ginty, Peripheral mechanosensory neuron dysfunction underlies tactile and behavioral deficits in mouse models of ASDs. *Cell* **166**, 299–313 (2016).
69. H. Oh, S. Lee, Y. Oh, S. Kim, Y. S. Kim, Y. Yang, W. Choi, Y.-E. Yoo, H. Cho, S. Lee, E. Yang, W. Koh, W. Won, R. Kim, C. J. Lee, H. Kim, H. Kang, J. Y. Kim, T. Ku, S.-B. Paik, E. Kim, Kv7/KCNQ potassium channels in cortical hyperexcitability and juvenile seizure-related death in Ank2-mutant mice. *Nat. Commun.* **14**, 3547 (2023).
70. S. Poliak, L. Gollan, R. Martinez, A. Custer, S. Einheber, J. L. Salzer, J. S. Trimmer, P. Shrager, E. Peles, Caspr2, a new member of the neurexin superfamily, is localized at the juxtaparanodes of myelinated axons and associates with K^+ channels. *Neuron* **24**, 1037–1047 (1999).
71. S. Poliak, D. Salomon, H. Elhanany, H. Sabanay, B. Kiernan, L. Pevny, C. L. Stewart, X. Xu, S.-Y. Chiu, P. Shrager, A. J. W. Furley, E. Peles, Juxtaparanodal clustering of Shaker-like K^+ channels in myelinated axons depends on Caspr2 and TAG-1. *J. Cell Biol.* **162**, 1149–1160 (2003).
72. R. Gao, N. H. Piguel, A. E. Melendez-Zaidi, M. D. Martin-de-Saavedra, S. Yoon, M. P. Forrest, K. Myczek, G. Zhang, T. A. Russell, J. G. Csernansky, D. J. Surmeier, P. Penzes, CNTNAP2 stabilizes interneuron dendritic arbors through CASK. *Mol. Psychiatry* **23**, 1832–1850 (2018).
73. ISH Data:: Allen Brain Atlas: Mouse Brain; https://mouse.brain-map.org/.
74. Q. You, Z. Luo, Z. Luo, Y. Kong, Z. Li, J. Yang, X. Li, T. Gao, Involvement of the thalamic reticular nucleus in prepulse inhibition of acoustic startle. *Transl. Psychiatry* **11**, 241 (2021).
75. R. Ayub, K. L. Sun, R. E. Flores, V. T. Lam, B. Jo, M. Saggar, L. K. Fung, Thalamocortical connectivity is associated with autism symptoms in high-functioning adults with autism and typically developing adults. *Transl. Psychiatry* **11**, 93 (2021).
76. G. Avanzini, M. de Curtis, F. Panzica, R. Spreafico, Intrinsic properties of nucleus reticularis thalami neurones of the rat studied in vitro. *J. Physiol.* **416**, 111–122 (1989).
77. L. Cueni, M. Canepari, R. Luján, Y. Emmenegger, M. Watanabe, C. T. Bond, P. Franken, J. P. Adelman, A. Lüthi, T-type Ca^{2+} channels, SK2 channels and SERCAs gate sleep-related oscillations in thalamic dendrites. *Nat. Neurosci.* **11**, 683–692 (2008).
78. J. R. Huguenard, D. A. McCormick, Thalamic synchrony and dynamic regulation of global forebrain oscillations. *Trends Neurosci.* **30**, 350–356 (2007).

Downloaded from https://www.science.org at Stanford University on August 25, 2025

79. M. Steriade, D. A. McCormick, T. J. Sejnowski, Thalamocortical oscillations in the sleeping and aroused brain. *Science* **262**, 679–685 (1993).
80. C. R. Houser, J. E. Vaughn, R. P. Barber, E. Roberts, GABA neurons are the major cell type of the nucleus reticularis thalami. *Brain Res.* **200**, 341–354 (1980).
81. B. Zikopoulos, H. Barbas, Altered neural connectivity in excitatory and inhibitory cortical circuits in autism. *Front. Hum. Neurosci.* **7**, 609 (2013).
82. F. Filice, L. Janickova, T. Henzi, A. Bilella, B. Schwaller, The parvalbumin hypothesis of autism spectrum disorder. *Front. Cell. Neurosci.* **14**, 577525 (2020).
83. D. Vogt, K. K. A. Cho, S. M. Shelton, A. Paul, Z. J. Huang, V. S. Sohal, J. L. R. Rubenstein, Mouse Cntnap2 and human CNTNAP2 ASD alleles cell autonomously regulate PV^{+} cortical interneurons. *Cereb. Cortex* **28**, 3868–3879 (2018).
84. M. Thabault, C. Fernandes-Gomes, A.-L. Huot, M. Francheteau, A. Balbous-Gautier, P.-O. Fernagut, L. Galvan, Dysfunction of striatal parvalbumin interneurons drives motor stereotypies in $Cntnap2^{-/-}$ mouse model of autism spectrum disorders. *PNAS Nexus* **3**, pgae132 (2024).
85. V. Marlinski, I. N. Beloozerova, Burst firing of neurons in the thalamic reticular nucleus during locomotion. *J. Neurophysiol.* **112**, 181–192 (2014).
86. J. R. Huguenard, Low-voltage-activated (T-type) calcium-channel genes identified. *Trends Neurosci.* **21**, 451–452 (1998).
87. M. Kleiman-Weiner, M. P. Beenhakker, W. A. Segal, J. R. Huguenard, Synergistic roles of $GABA_A$ receptors and SK channels in regulating thalamocortical oscillations. *J. Neurophysiol.* **102**, 203–213 (2009).
88. T. Zaman, K. Lee, C. Park, A. Paydar, J. H. Choi, E. Cheong, C. J. Lee, H.-S. Shin, CaV2.3 channels are critical for oscillatory burst discharges in the reticular thalamus and absence epilepsy. *Neuron* **70**, 95–108 (2011).
89. T. Bal, D. A. McCormick, Mechanisms of oscillatory activity in guinea-pig nucleus reticularis thalami in vitro: A mammalian pacemaker. *J. Physiol.* **468**, 669–691 (1993).
90. A. T.-H. Lu, X. Dai, J. A. Martinez-Agosto, R. M. Cantor, Support for calcium channel gene defects in autism spectrum disorders. *Mol. Autism.* **3**, 18 (2012).
91. E. M. Talley, L. L. Cribbs, J. H. Lee, A. Daud, E. Perez-Reyes, D. A. Bayliss, Differential distribution of three members of a gene family encoding low voltage-activated (T-type) calcium channels. *J. Neurosci.* **19**, 1895–1911 (1999).
92. S. E. Lee, J. Lee, C. Latchoumane, B. Lee, S.-J. Oh, Z. A. Saud, C. Park, N. Sun, E. Cheong, C.-C. Chen, E.-J. Choi, C. J. Lee, H.-S. Shin, Rebound burst firing in the reticular thalamus is not essential for pharmacological absence seizures in mice. *Proc. Natl. Acad. Sci. U.S.A.* **111**, 11828–11833 (2014).
93. M. C. Iftinca, G. W. Zamponi, Regulation of neuronal T-type calcium channels. *Trends Pharmacol. Sci.* **30**, 32–40 (2009).
94. Y. Zhang, X. Jiang, T. P. Snutch, J. Tao, Modulation of low-voltage-activated T-type Ca^{2+} channels. *Biochim. Biophys. Acta* **1828**, 1550–1559 (2013).
95. E. K. Harding, A. Dedek, R. P. Bonin, M. W. Salter, T. P. Snutch, M. E. Hildebrand, The T-type calcium channel antagonist, Z944, reduces spinal excitability and pain hypersensitivity. *Br. J. Pharmacol.* **178**, 3517–3532 (2021).
96. A. J. Roebuck, W. N. Marks, M. C. Liu, N. B. Tahir, N. K. Zabder, T. P. Snutch, J. G. Howland, Effects of the T-type calcium channel antagonist Z944 on paired associates learning and locomotor activity in rats treated with the NMDA receptor antagonist MK-801. *Psychopharmacology* **235**, 3339–3350 (2018).
97. M. T. Tse, A class of its own. *Nat. Rev. Drug Discov.* **11**, 274–274 (2012).
98. W. N. Marks, N. K. Zabder, S. M. Cain, T. P. Snutch, J. G. Howland, The T-type calcium channel antagonist, Z944, alters social behavior in Genetic Absence Epilepsy Rats from Strasbourg. *Behav. Brain Res.* **361**, 54–64 (2019).
99. J. R. Huguenard, D. A. Prince, Intrathalamic rhythmicity studied in vitro: Nominal T-current modulation causes robust antioscillatory effects. *J. Neurosci.* **14**, 5485–5502 (1994).
100. R. Jagirdar, C.-H. Fu, J. Park, B. F. Corbett, F. M. Seibt, M. Beierlein, J. Chin, Restoring activity in the thalamic reticular nucleus improves sleep architecture and reduces Aβ accumulation in mice. *Sci. Transl. Med.* **13**, eabh4284 (2021).
101. A. Destexhe, D. Contreras, M. Steriade, T. J. Sejnowski, J. R. Huguenard, In vivo, in vitro, and computational analysis of dendritic calcium currents in thalamic reticular neurons. *J. Neurosci.* **16**, 169–185 (1996).
102. J. T. Paz, C. A. Christian, I. Parada, D. A. Prince, J. R. Huguenard, Focal cortical infarcts alter intrinsic excitability and synaptic excitation in the reticular thalamic nucleus. *J. Neurosci.* **30**, 5465–5479 (2010).
103. A. S. Bryant, B. Li, M. P. Beenhakker, J. R. Huguenard, Maintenance of thalamic epileptiform activity depends on the astrocytic glutamate-glutamine cycle. *J. Neurophysiol.* **102**, 2880–2888 (2009).
104. V. S. Sohal, J. R. Huguenard, Inhibitory interconnections control burst pattern and emergent network synchrony in reticular thalamus. *J. Neurosci.* **23**, 8978–8988 (2003).
105. Y.-D. Li, Y.-J. Luo, Z.-K. Chen, L. Quintanilla, Y. Cherasse, L. Zhang, M. Lazarus, Z.-L. Huang, J. Song, Hypothalamic modulation of adult hippocampal neurogenesis in mice confers activity-dependent regulation of memory and anxiety-like behavior. *Nat. Neurosci.* **25**, 630–645 (2022).

Acknowledgments: We thank all current lab members for feedback during the entire project. We also thank N. Agranonik for managing mouse lines, laboratory equipment, and supplies. **Funding:** This work was supported by SFARI award no. 633450 and NIMH RO1 MH121075. **Author contributions:** Conceptualization: S.-S.J. and J.R.H. Methodology: S.-S.J., F.T., and J.R.H. Investigation: S.-S.J., F.T., and J.R.H. Visualization: S.-S.J. and F.T. Supervision: J.R.H. Writing—original draft: S.-S.J. Writing—review and editing: S.-S.J. and J.R.H. Funding acquisition: J.R.H. **Competing interests:** The authors declare that they have no competing interests. **Data and materials availability:** All data needed to evaluate the conclusions in the paper are present in the paper and/or the Supplementary Materials.

Submitted 22 March 2025
Accepted 23 July 2025
Published 20 August 2025
10.1126/sciadv.adw4682

Downloaded from https://www.science.org at Stanford University on August 25, 2025